Exploring lepton flavor violation phenomena of the Z and Higgs bosons at electron-proton colliders

Adil Jueid[*]
Center for Theoretical Physics of the Universe, Institute for Basic Science (IBS),
Daejeon, 34126, Republic of Korea

Jinheung Kim,[†] Soojin Lee,[‡] Jeonghyeon Song,[§] and Daohan Wang[∥]
Department of Physics, Konkuk University, Seoul 05029, Republic of Korea

(Received 20 May 2023; revised 8 July 2023; accepted 30 August 2023; published 20 September 2023)

We conduct a comprehensive analysis of the potential for discovering lepton flavor violation (LFV) phenomena associated with the Z and Higgs bosons at the LHeC and FCC-he. Our thorough investigation highlights the exceptional suitability of electron-proton colliders for probing these rare new physics signals, due to their distinct advantages, such as negligible pileups, minimal QCD backgrounds, electron-beam polarization P_e, and the ability to distinguish charged-current from neutral-current processes. In our analysis of LFV of the Z boson, we employ an innovative indirect probe, utilizing the t-channel mediation of the Z boson in the process $pe^- \to j\tau^-$. For LFV in the Higgs sector, we examine direct observations of the on-shell decays of $H \to e^+\tau^-$ and $H \to \mu^\pm\tau^\mp$ through the charged-current production of H. Focusing on $H \to e^+\tau^-$ is highly efficient due to the absence of positron-related backgrounds in the charged-current modes at electron-proton colliders. Through a dedicated signal-to-background analysis using the boosted decision tree algorithm, we show that the LHeC with a total integrated luminosity of $1\ \mathrm{ab}^{-1}$ can establish significantly lower 2σ bounds than the HL-LHC with $3\ \mathrm{ab}^{-1}$. Specifically, we find $\mathrm{Br}(Z \to e\tau) < 2.2 \times 10^{-7}$, $\mathrm{Br}(H \to e\tau) < 1.7 \times 10^{-4}$, and $\mathrm{Br}(H \to \mu\tau) < 1.0 \times 10^{-4}$ when we apply the optimal cut on the boosted decision tree output. Furthermore, our study reveals the exceptional precision of the FCC-he in measuring the LFV signatures of the Z and Higgs bosons, indicating a promising potential for future discoveries in this fascinating field.

DOI: 10.1103/PhysRevD.108.055024

I. INTRODUCTION

Particle physics has made tremendous progress in the past few decades with the success of the Standard Model (SM) in explaining almost all experiments, including the discovery of the Higgs boson [1,2]. However, we are still on a quest for the ultimate theory of the Universe, driven by two main reasons. First, the SM falls short in addressing fundamental questions that remain unanswered in our understanding of the universe. These include the nature of dark matter [3,4], the naturalness problem [5–7], the origin of neutrino masses, baryogenesis, and the metastability of the SM vacuum [8]. Second, tantalizing clues of physics beyond the SM (BSM) have surfaced. Noteworthy examples include the muon anomalous magnetic moment [9–11], the CDF W-boson mass [12], the Cabibbo angle anomaly [13–15], the excess in the diphoton mode around 96 GeV [16], and the multilepton anomalies [17–19]. Any conclusive indication of BSM physics will bring new insights to our quest.

The study of lepton flavor violation (LFV) offers a remarkably clean pathway to explore BSM. In the SM, LFV is highly suppressed due to the Glashow-Iliopoulos-Maiani cancellation mechanism and the tiny neutrino masses [20]. However, the observation of neutrino oscillations reveals that lepton flavor is not an exact symmetry, making LFV an elusive yet captivating realm to investigate. Numerous BSM models have been proposed to accommodate LFV, such as massive neutrino models [21–29], multi-Higgs doublet models [30–33], supersymmetric models [34,35,35,36], composite Higgs models [37], warped dimensional models [38–40], SMEFT [41], and dark matter models [42,43]. LFV signals can manifest at

---

[*] adiljueid@ibs.re.kr
[†] jinheung.kim1216@gmail.com
[‡] soojinlee957@gmail.com
[§] jhsong@konkuk.ac.kr
[∥] wdh9508@gmail.com

TABLE I. The current status and future prospects of the direct bounds on the LFV decays of Z and the Higgs boson at the 95% C.L. The prospects for the FCC-ee-Z collider are based on the configuration with $\sqrt{s} = 88$–95 GeV and $\mathcal{L} = 150\ \mathrm{ab}^{-1}$, while those for the e^+e^- collider are for $\sqrt{s} = 240$ GeV and $\mathcal{L} = 5\ \mathrm{ab}^{-1}$.

	Current	Future		Current	Future	
$\mathrm{Br}(Z \to e\mu)$	$< 2.62 \times 10^{-7}$ ATLAS [50]	$\lesssim 10^{-8}$ FCC-ee-Z [51]	$\mathrm{Br}(H \to e\mu)$	$< 4.4 \times 10^{-5}$ CMS [52]	$< \mathcal{O}(0.02)\%$ HL-LHC [53]	$< 1.2 \times 10^{-5}$ e^+e^- collider [54]
$\mathrm{Br}(Z \to e\tau)$	$< 5.0 \times 10^{-6}$ ATLAS [55]	$\lesssim 10^{-9}$ FCC-ee-Z [51]	$\mathrm{Br}(H \to e\tau)$	$< 2.0 \times 10^{-3}$ ATLAS [56]	$< \mathcal{O}(0.5)\%$ HL-LHC [53]	$< 1.6 \times 10^{-4}$ e^+e^- collider [54]
$\mathrm{Br}(Z \to \mu\tau)$	$< 6.5 \times 10^{-6}$ ATLAS [55]	$\lesssim 10^{-9}$ FCC-ee-Z [51]	$\mathrm{Br}(H \to \mu\tau)$	$< 1.5 \times 10^{-3}$ CMS [57]	$< 1.0 \times 10^{-3}$ HL-LHC [58]	$\lesssim 1.4 \times 10^{-4}$ e^+e^- collider [54]

low energy scales through the rare LFV decays of leptons and mesons, such as $\mu \to e\gamma$, $\mu \to eee$, $\tau \to e\gamma/\mu\gamma$, $\mu \to e$ conversion in nuclei, and $\pi^0 \to \mu e$ [44]. Another intriguing category involves the LFV decays of the Z or Higgs boson, $Z \to L_\alpha L_\beta$ and $H \to L_\alpha L_\beta$ ($\alpha \neq \beta$) where $L_{\alpha,\beta} = e, \mu, \tau$. In this work, we focus on the latter, as they present an enchanting research area within the context of high-energy colliders.

To provide a comprehensive overview of this intriguing topic, we present in Table I the current status and future prospects for the branching ratios of LFV decays of the Z and Higgs boson at the 95% confidence limit (C.L.) based on direct constraints. Notably, the $e\mu$ mode is stringently constrained by indirect measurements, such that $\mathrm{Br}(Z \to e\mu) \lesssim 10^{-12}$ from $\mu \to eee$ [41,45] and $\mathrm{Br}(H \to e\mu) < \mathcal{O}(10^{-8})$ [46–48] from $\mu \to e\gamma$ [49]. However, the $e\tau$ and $\mu\tau$ modes still offer the possibility of sizable branching ratios, indicating the potential for groundbreaking discoveries of LFV at high-energy colliders.

Another important observation from Table I is that electron-proton colliders, such as the Large Hadron electron Collider (LHeC) [59–61] and the Future Circular Collider electron-proton option (FCC-he) [62], have not been considered for LFV studies of the Z and Higgs bosons. The next-generation electron-proton colliders will play a crucial role in future high-energy hadron colliders, offering a unique advantage in providing high-precision data for accurately determining parton distribution functions of a proton. In particular, the LHeC merits special attention due to its ability to operate simultaneously with the HL-LHC, made possible by the development of the energy recovery linac for the electron beam [61].

Unfortunately, the distinct advantages of electron-proton colliders in detecting rare BSM events have not been fully acknowledged in the existing literatures. For instance, the electron beam mitigates issues related to pileup collisions. This becomes crucial when probing rare BSM events, which can be overshadowed at the HL-LHC by the presence of over 150 pileup collisions per event. The LHeC (FCC-he) offers a clean environment with approximately 0.1 (1) pileup collisions. Additionally, electron-proton colliders provide a high level of control over backgrounds by disentangling the charged-current (CC) and neutral-current (NC) processes and enabling forward direction identification. Another advantage lies in the electron beam polarization P_e, which amplifies the cross sections in the CC channels.

These unique merits make electron-proton colliders exceptionally well suited for investigating LFV signatures of the Z and Higgs bosons. Although directly measuring the decay of $Z \to e\tau/\mu\tau$ poses significant challenges due to their minuscule branching ratios below $\mathcal{O}(10^{-6})$, the electron beam provides an ingenious indirect probe through the process $pe^- \to j\tau^-$ mediated by the Z boson in the t-channel diagram. To assess the sensitivity of this indirect channel, we will conduct a comprehensive detector simulation employing both a cut-based analysis and a boosted decision tree (BDT) analysis [63].

For the $H \to e\tau$ mode, our focus will be on $H \to e^+\tau^-$ via the CC channel, taking advantage of the absence of the positron-related backgrounds. Encouragingly, the $H \to \mu^\pm\tau^\mp$ mode also benefits from a low background environment. Given the extremely small production cross sections of the Higgs boson at the LHeC and FCC-he, we will utilize a BDT analysis to enhance the signal-to-background discrimination and extract valuable information from the limited number of events. Our analysis will reveal that the proposed channels at the LHeC with a total integrated luminosity of $\mathcal{L}_{\mathrm{tot}} = 1\ \mathrm{ab}^{-1}$ yield significantly lower bounds on the branching ratios than the projected bounds at the HL-LHC with $\mathcal{L}_{\mathrm{tot}} = 3\ \mathrm{ab}^{-1}$. Furthermore, the FCC-he exhibits even greater potential in this regard. These findings represent a novel and significant contribution to the topic, highlighting the untapped potential of electron-proton colliders in probing the LFV phenomena.

The paper is structured as follows: In Sec. II, we provide a model-independent formalism for the LFV phenomena of the Z and Higgs bosons. After calculating the production cross sections of H, Z, $W^\pm$, and $jj\nu$ in the SM, we discuss all the possible channels to probe the LFV signatures at electron-proton colliders. Based on this, we propose the most promising channels. In Sec. III, we present our signal-to-background analysis using a full detector simulation. Finally, we summarize our findings and conclusions in Sec. IV.

II. FORMALISM

In our exploration of LFV signatures associated with the Z and Higgs bosons at electron-proton colliders, we employ a model-independent approach. To characterize LFV in the Z boson sector, we consider the following LFV couplings involving the Z boson, an electron, and a tau lepton:

$$-\mathcal{L}^{Z}_{\mathrm{LFV}} = Z_\mu \Big[\bar{\tau}\gamma^\mu (C^L_{\tau e} P_L + C^R_{\tau e} P_R) e + \bar{e}\gamma^\mu (C^L_{e\tau} P_L + C^R_{e\tau} P_R)\tau \Big], \tag{1}$$

where $P_{R,L} = (1 \pm \gamma^5)/2$. The couplings $C^{L,R}_{e\tau,\tau e}$ are connected to the LFV branching ratio according to

$$|C^L_{\tau e}|^2 + |C^R_{\tau e}|^2 + |C^L_{e\tau}|^2 + |C^R_{e\tau}|^2 = \frac{24\pi\Gamma^{\mathrm{tot}}_Z}{m_Z} \mathrm{Br}(Z \to e\tau). \tag{2}$$

In this study, our focus lies on the indirect process utilizing the t-channel mediation of the Z boson in the process $pe^- \to j\tau^-$, which examines the couplings $C^{L/R}_{\tau e}$. However, it is necessary to reinterpret the current limit of $\mathrm{Br}(Z \to e\tau) < 5.0 \times 10^{-6}$ in terms of $C^{L,R}_{\tau e}$. We take a reasonable assumption of $|C^{L/R}_{\tau e}| = |C^{L/R}_{e\tau}|$ and obtain the constraint of

$$\sqrt{|C^R_{\tau e}|^2 + |C^L_{\tau e}|^2} < 2.27 \times 10^{-3}. \tag{3}$$

Regarding the LFV Yukawa couplings of the Higgs boson, we introduce the following interaction Lagrangian:

$$-\mathcal{L}^{H}_{\mathrm{LFV}} = Y_{\alpha\beta} \bar{L}_\alpha P_R L_\beta H + \mathrm{H.c.}, \quad (\alpha \neq \beta), \tag{4}$$

where $L_{\alpha,\beta} = e,\ \mu,\ \tau$. The relationship between $Y_{\alpha\beta}$ and $\mathrm{Br}(H \to L_\alpha L_\beta)$ is given by

$$|Y_{\alpha\beta}|^2 + |Y_{\beta\alpha}|^2 = \frac{8\pi}{m_H} \frac{\mathrm{Br}(H \to L_\alpha L_\beta)}{1 - \mathrm{Br}(H \to L_\alpha L_\beta)} \Gamma^{\mathrm{tot}}_H. \tag{5}$$

The current constraints of $\mathrm{Br}(H \to e\tau) < 2.2 \times 10^{-3}$ and $\mathrm{Br}(H \to \mu\tau) < 1.5 \times 10^{-3}$ imply

$$\begin{aligned} \sqrt{|Y_{e\tau}|^2 + |Y_{\tau e}|^2} &< 1.30 \times 10^{-3}, \\ \sqrt{|Y_{\mu\tau}|^2 + |Y_{\tau\mu}|^2} &< 1.13 \times 10^{-3}. \end{aligned} \tag{6}$$

Before delving into the potential channels to discover the LFV signatures at electron-proton colliders, it is useful to summarize the total production cross sections of the Higgs boson, $W^\pm$, Z, and two QCD jets in the SM. Table II presents the cross sections at the LHeC and FCC-he, with the configurations of

$$\begin{aligned} &\text{LHeC:}\ E_e = 50\ \text{GeV}, \qquad E_p = 7\ \text{TeV}, \\ &\text{FCC-he:}\ E_e = 60\ \text{GeV}, \qquad E_p = 50\ \text{TeV}. \end{aligned} \tag{7}$$

TABLE II. The SM cross sections in units of pb for the productions of H, $W^\pm$, Z, and two jets at the LHeC and FCC-he. Here j_{f} denotes the forward jet and e^-_{b} the backward electron. The values are based on the parton-level calculation in the four-flavor scheme for protons. The kinematic phase space is constrained by $p_T^{e,j} > 10$ GeV, $|\eta_{e,j}| < 5$, and $\Delta R_{ej,jj} > 0.4$.

Total SM cross sections in pb at the LHeC with $E_e = 50$ GeV and $E_p = 7$ TeV

		Higgs	$W^\pm$		Z	Multijets
CC		$\sigma(H + j_{\mathrm{f}}\nu_e)$	$\sigma(W^- + j_{\mathrm{f}}\nu_e)$	$\sigma(W^+ + j_{\mathrm{f}}\nu_e)$	$\sigma(Z + j_{\mathrm{f}}\nu_e)$	$\sigma(jj\nu_e)$
	$P_e = 0$	0.081	0.925	0	0.456	72.53
	$P_e = -80\%$	0.145	1.657	0	0.824	130.9
NC		$\sigma(H + j_{\mathrm{f}}e^-_{\mathrm{b}})$	$\sigma(W^- + j_{\mathrm{f}}e^-_{\mathrm{b}})$	$\sigma(W^+ + j_{\mathrm{f}}e^-_{\mathrm{b}})$	$\sigma(Z + j_{\mathrm{f}}e^-_{\mathrm{b}})$	$\sigma(jje^-_{\mathrm{b}})$
	$P_e = 0$	0.0144	1.031	1.112	0.244	961.0
	$P_e = -80\%$	0.0171	1.433	1.478	0.3138	1019

Total SM cross sections in pb at the FCC-he with $E_e = 60$ GeV and $E_p = 50$ TeV

CC		$\sigma(H + j_{\mathrm{f}}\nu_e)$	$\sigma(W^- + j_{\mathrm{f}}\nu_e)$	$\sigma(W^+ + j_{\mathrm{f}}\nu_e)$	$\sigma(Z + j_{\mathrm{f}}\nu_e)$	$\sigma(jj\nu_e)$
	$P_e = 0$	0.335	4.253	0	2.205	235.2
	$P_e = -80\%$	0.604	7.618	0	3.969	424
NC		$\sigma(H + j_{\mathrm{f}}e^-_{\mathrm{b}})$	$\sigma(W^- + j_{\mathrm{f}}e^-_{\mathrm{b}})$	$\sigma(W^+ + j_{\mathrm{f}}e^-_{\mathrm{b}})$	$\sigma(Z + j_{\mathrm{f}}e^-_{\mathrm{b}})$	$\sigma(jje^-_{\mathrm{b}})$
	$P_e = 0$	0.0766	4.746	4.373	0.806	2972
	$P_e = -80\%$	0.0906	6.826	5.940	1.042	3157

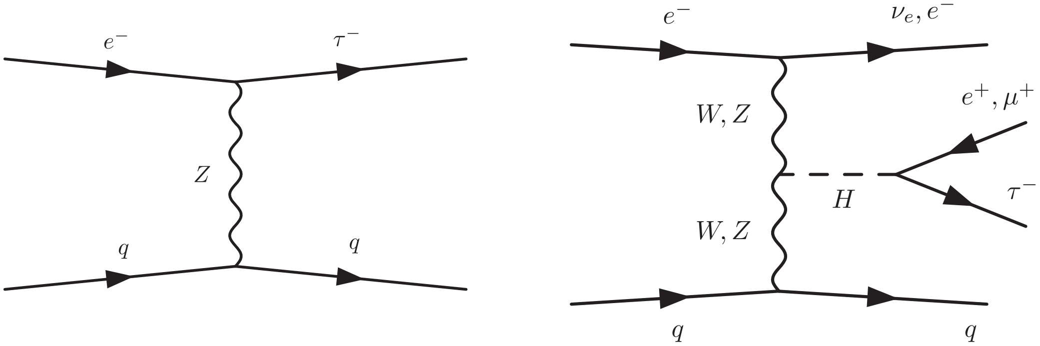

FIG. 1. Feynman diagrams for the LFV signal of the Z boson (left panel) and the Higgs boson (right panel) at electron-proton colliders.

We used MadGraph5_aMC@NLO [64] with four-flavor scheme and `NNPDF31_lo` parton distribution function set for a proton [65]. We classified the processes in two categories, the CC and NC processes. In the CC process, a forward[1] jet j_f accompanies a backward neutrino, while the NC process involves a backward electron e_b^- and a forward jet j_f. Two choices for the electron beam polarization, $P_e = 0$ and $P_e = -80\%$, are also considered.

In terms of production mechanisms, the Higgs boson, $W^\pm$, and Z undergo vector boson fusion, except for the NC production of the Z boson. As a result, the production cross sections are generically small, around $\mathcal{O}(1)$ pb for the $W^\pm/Z$ production and $\mathcal{O}(0.1)$ pb for the Higgs boson production at the LHeC. Despite the higher proton beam energy at the FCC-he, there is no significant enhancement in the production cross sections due to the dependence on the square of the center-of-mass energy, $s = 4E_e E_p$. On the other hand, the electron beam polarization has a considerable impact on the production cross sections. When $P_e = -80\%$, the CC production cross section experiences an enhancement by a factor of approximately 1.8. However, the increase in the NC production cross section is smaller. Given the inherently small LFV signal rate, therefore, the CC production channel becomes a more efficient choice to improve the sensitivity of the BSM search.

It is worth noting that the QCD multijet backgrounds of $jj\nu$ and jje_b^- do not give rise to a forward jet, because an additional jet radiates from the initial or final quark/gluon. Another unique feature of electron-proton colliders is the absence of prompt W^+ production in the CC channel. Furthermore, in the case of single top quark production, only the antitop quark can be produced through the CC process, and its decay products do not include a W^+ boson. These unique features assist in suppressing the backgrounds for LFV signals involving the Z and Higgs bosons.

We now explore the potential channels for detecting the LFV phenomena in the Z sector. Unfortunately, conducting direct searches for the on-shell decay of $Z \to L_\alpha L_\beta$ is unfeasible at the LHeC and FCC-he. At the LHeC, the total production cross sections of a Z boson even with $P_e = -80\%$ are 824 fb and 314 fb in the CC and NC channels, respectively. The extremely small branching ratios of $Z \to L_\alpha L_\beta$ listed in Table I make it impossible to achieve observable event rates with the anticipated total luminosity of 1 ab^{-1}.

Fortunately, we can indirectly investigate the Z-e-τ vertex through the t-channel mediation of the Z boson by exploiting the initial electron beam.[2] Our proposed process is as follows:

$$p + e^- \to j_\mathrm{f} + \tau^-. \tag{8}$$

The corresponding Feynman diagram is depicted in the left panel of Fig. 1. The final state comprises one forward jet and one backward tau lepton with negative electric charge. The tau lepton can be identified if it decays hadronically because the tau jet yields a fewer particle multiplicity and a localized energy deposit [67–69]. We will use the notation τ_h for the hadronically decaying tau lepton in what follows. The NC backgrounds are easily suppressed by vetoing the event with an electron. The primary background originates from the QCD process $jj\nu_e$ in the CC mode, where one jet is mistagged as τ_h. The second dominant background arises from the CC process of $pe^- \to W^- + j_\mathrm{f}\nu_e$, followed by $W^- \to \tau^-\nu_\tau$. Additionally, we will consider the CC process of $Z(\to \tau^+\tau^-) + j_\mathrm{f}\nu_e$, where one tau lepton escapes detection.

In the study of LFV phenomena of the Higgs boson, we can consider two types of processes: direct decays $H \to e\tau/\mu\tau$ and an indirect process $e^-p \to \tau^- j$ mediated by the Higgs boson in the t-channel. However, the indirect process is subject to significant suppression due to the extremely small Yukawa couplings between the Higgs boson and leptons, as well as the loop-induced couplings of the Higgs boson to gluons. As a result, our primary focus is directed toward the on-shell decays of the Higgs boson.

---

[1] Note that the direction of the proton beam is defined as forward.

[2] The LFV of a Z' boson through the t-channel at the LHeC was studied in Ref. [66].

TABLE III. The signal and background processes of the LFV phenomena of the Z and Higgs bosons at electron-proton colliders. Here τ_ℓ denotes the tau lepton decaying into $\ell\nu_\ell\nu_\tau$ ($\ell = e, \mu$), τ_h is the hadronically decaying τ, j_X is the QCD jet mistagged as the particle X, and τ_un is the tau lepton escaping the detection.

			Signal	Backgrounds
LFV Z	$e\tau$	NC	$j_\mathrm{f}\tau^-$	$W^-(\to \tau^-\nu)/Z(\to \tau\tau_\mathrm{un}) + j_\mathrm{f}\nu,\ jj_{\tau_\mathrm{h}}\nu$
LFV H	$e\tau$	CC	$H(\to e^+\tau^-) + j_\mathrm{f}\nu$	$Z(\to \tau_{e^+}\tau_\mathrm{h}) + j_\mathrm{f}\nu,\ j_e j_{\tau_\mathrm{h}} + j_\mathrm{f}\nu$
		NC	$H(\to e^\pm\tau^\mp) + j_\mathrm{f}e_\mathrm{b}^-$	$Z(\to \tau_e\tau_\mathrm{h})/W^\pm(\to j_e j_{\tau_\mathrm{h}})/H(\to \tau_e\tau_\mathrm{h}) + j_\mathrm{f}e_\mathrm{b}^-$ $W^\pm(\to e^\pm\nu)j_\tau + j_\mathrm{f}e_\mathrm{b}^-$
	$\mu\tau$	CC	$H(\to \mu^\pm\tau^\mp) + j_\mathrm{f}\nu$	$Z(\to \tau_\mu\tau_\mathrm{h})/H(\to \tau_\mu\tau_\mathrm{h}) + j_\mathrm{f}\nu$
		NC	$H(\to \mu^\pm\tau^\mp) + j_\mathrm{f}e_\mathrm{b}^-$	$Z(\to \tau_\mu\tau_\mathrm{h})/H(\to \tau_\mu\tau_\mathrm{h}) + j_\mathrm{f}e_\mathrm{b}^-$

For the decay of $H \to e\tau$, let us first consider the CC production of the Higgs boson. As shown in Table II, the CC production of W^+, which could yield the significant background to the positron final state, vanishes at the leading order. Therefore, we propose the signal process of

$$p + e^- \to H(\to e^+\tau^-) + j_\mathrm{f}\nu_e, \tag{9}$$

of which the final state consists of a positron, a negatively charged τ_h, a forward jet, and a backward neutrino. The Feynman diagram is in the right panel of Fig. 1. Two backgrounds contribute. The primary one arises from $pe^- \to Z + j_\mathrm{f}\nu_e$ followed by $Z \to \tau_{e^+}\tau_\mathrm{h}{}^-$ or $Z \to j_{e^+}j_{\tau_\mathrm{h}}$. Here τ_{e^+} represents the tau lepton decaying into $\tau^+ \to e^+\nu_e\bar{\nu}_\tau$, and j_X is a QCD jet mistagged as the particle X. The second dominant background is associated with the production of multiple jets and a neutrino, $pe^- \to j_{e^+}j_{\tau_\mathrm{h}} + j_\mathrm{f}\nu_e$, where one jet is mistagged as a positron and the other jet is mistagged as τ_h.

To explore the NC process of $H \to e\tau$, we propose incorporating both $H \to e^+\tau^-$ and $H \to e^-\tau^+$ due to the small NC production cross section. The suggested process is as follows:

$$p + e^- \to H(\to e^\pm\tau^\mp) + j_\mathrm{f}e_\mathrm{b}^-. \tag{10}$$

In this case, the final state consists of an electron/positron, τ_h, a forward jet, and the backward electron. The primary background stems from $pe^- \to Z + j_\mathrm{f}e_\mathrm{b}^-$, followed by $Z \to \tau_e\tau_\mathrm{h}$ or $Z \to j_e j_{\tau_\mathrm{h}}$. Another significant backgrounds arise from the NC processes of $pe^- \to W^\pm(\to e^\pm\nu)j_\tau + j_\mathrm{f}e_\mathrm{b}^-$ and $pe^- \to W^\pm(\to j_e j_\tau) + j_\mathrm{f}e_\mathrm{b}^-$. Lastly, there is a background from $pe^- \to H + j_\mathrm{f}e_\mathrm{b}^-$, followed by $H \to \tau_e\tau_\mathrm{h}$. The backgrounds originating from the CC processes can be efficiently suppressed by vetoing events with missing transverse energy (E_T^miss) and requiring a backward electron.

For the decay of $H \to \mu\tau$ in the CC mode, we consider the final state consisting of a muon (regardless of its electric charge), a tau lepton, the missing transverse energy, and a forward jet. As there is no electron in the signal event, the NC background processes are easily controlled. Among the CC processes, the dominant background originates from $pe^- \to Z + j_\mathrm{f}\nu_e$ followed by $Z \to \tau_\mu\tau_\mathrm{h}$. The second background arises from $pe^- \to H + j_\mathrm{f}\nu$, followed by $H \to \tau_\mu\tau_\mathrm{h}$. In the NC signal process of $H \to \mu\tau$, the final state comprises a muon, a tau lepton, a backward electron, and a forward jet. The main background is from $pe^- \to Z + j_\mathrm{f}e_\mathrm{b}^-$, followed by $Z \to \tau_\mu\tau_\mathrm{h}$. The subleading background comes from $pe^- \to H + j_\mathrm{f}e_\mathrm{b}^-$, followed by $H \to \tau_\mu\tau_\mathrm{h}$.

In Table III, we summarize the potential discovery channels to probe the LFV phenomena of the Z and Higgs bosons along with the corresponding backgrounds. Regarding the LFV of the Z boson, the only feasible option at electron-proton colliders is the indirect probe through the process $pe^- \to j_\mathrm{f}\tau^-$. For the LFV in the H sector, we suggest two decay modes of $H \to e^+\tau^-$ and $H \to \mu^\pm\tau^\mp$ in the CC production of the Higgs boson because the NC mode has a few disadvantages. First, the NC production cross section of the Higgs boson is merely about 10% of the CC production cross section, as shown in Table II. Second, the electron beam polarization of $P_e = -80\%$ diminishes the discovery potential since the background cross sections of the NC production of Z and $W^\pm$ increase more than that of H.

Now we discuss the parton-level cross sections of the signals and backgrounds. For the signal, we first obtained the Universal FeynRules Output (UFO) [70] file for the BSM with the Lagrangian in Eqs. (1) and (4). The event generation at leading order is performed using MadGraph5_aMC@NLO [64] version 3.4.2 with `NNPDF31_lo` parton distribution function set [65]. The generator-level cuts were imposed on the parton-level objects like $p_T^j > 10$ GeV, $\Delta R_{ij} > 0.4$, and $|\eta_j| < 5$. Here $\Delta R = \sqrt{(\Delta\eta)^2 + (\Delta\phi)^2}$ with η and ϕ being the rapidity and azimuthal angle, respectively. For the renormalization and factorization scales, we take

$$\mu_{R,0} = \mu_{F,0} \equiv \frac{1}{2}\sum_i \sqrt{p_{T,i}^2 + m_i^2}, \tag{11}$$

where i covers all the particles in the final state.

By setting $C^L_{\tau e} = C^R_{\tau e} = 10^{-3}$, we calculated the parton-level cross sections of $pe^- \to j_\mathrm{f}\tau^-$ as

$$\begin{aligned}&\text{LHeC}:\ \sigma(pe^- \to j_\mathrm{f}\tau^-)|_{C^{L,R}_{\tau e}=10^{-3}}\\ &\quad= \begin{cases}1.29\ \text{fb} & \text{for}\ P_e = 0;\\ 1.31\ \text{fb} & \text{for}\ P_e = -80\%;\end{cases}\\ &\text{FCC-he}:\ \sigma(pe^- \to j_\mathrm{f}\tau^-)|_{C^{L,R}_{\tau e}=10^{-3}}\\ &\quad= \begin{cases}3.38\ \text{fb} & \text{for}\ P_e = 0;\\ 3.41\ \text{fb} & \text{for}\ P_e = -80\%.\end{cases}\end{aligned} \tag{12}$$

It is evident that the signal cross section is not significantly enhanced by $P_e = -80\%$. Since the cross sections for the main CC backgrounds increase by a factor of about 1.8, we set $P_e = 0$ for the LFV studies of Z. For the LFV phenomena of the Higgs boson, the signal cross sections of $pe^- \to H(\to e\tau/\mu\tau) + j_\mathrm{f}\nu$ can be obtained by multiplying the branching ratio and the Higgs production cross sections presented in Table II. If $\mathrm{Br}(H \to e\tau/\mu\tau) = 10^{-3}$, the total cross section of the signal with $P_e = -80\%$ is about 145ab at the LHeC and about 604 ab at the FCC-he.

III. SIGNAL-TO-BACKGROUND ANALYSIS

In this section, we conduct a comprehensive analysis of the signal and backgrounds through the full simulation at the detector level. The Monte Carlo event generation procedure is as follows. First, we employ MadGraph5_aMC@NLO to generate events for both the signal and backgrounds at leading order with parton distribution functions using the `NNPDF31_lo` PDF set and $\alpha_s(m_Z^2) = 0.118$. To accurately simulate the decays of $W^\pm$ and Z, as well as to account for parton showering and hadronization effects, we use PYTHIA version `8.309` [71]. In order to incorporate more stable performance of the PYTHIA for electron-proton colliders, we made some modifications to the default setup, setting `partonlevel:mpi=off`, `SpaceShower:dipoleRecoil=on`, `PDF:lepton=off`, and `TimeShower:QEDshowerByL=off`.

To simulate the detector effects, we utilized version 3.5.0 of DELPHES [72]. We adjust the DELPHES card[3] to align the particle efficiencies, momentum smearing, and isolation parameters with the default values specified in the LHeC Concept Design Report [61]. Jet clustering was performed using the anti-k_T algorithm [73] with a jet radius $R = 0.4$ implemented in `FastJet` version 3.3.4 [74].

The τ_h-tagging plays a crucial role in detecting the LFV signals of the Z and Higgs bosons. Let us elaborate on our strategy for choosing the τ_h-tagging efficiency in more detail. The τ_h-tagging efficiency is not fixed but rather a parameter that we can choose depending on our target process. When selecting the τ_h-tagging efficiency, it is essential to strike a balance between retaining the τ-related signal events and suppressing the background events. To find this balance, we take into account the feature that as the tagging efficiency increases, the mistagging rate also increases.

For the LFV Z channel, the primary background is $jj\nu$. Given that this background overwhelmingly dominates the signal, our primary objective is to effectively suppress the QCD background. To achieve this, we chose a relatively small τ_h-tagging efficiency. By doing so, we reduce the mistagging probability, thereby minimizing contamination from QCD jets and enhancing the sensitivity to the LFV Z signal. In our analysis, we have specifically chosen $P_{\tau_\mathrm{h}\to\tau_\mathrm{h}} = 0.4$ for the τ_h-tagging efficiency and $P_{j\to\tau_\mathrm{h}} = 0.001$ for the mistagging probability. These values are based on the default settings in the DELPHES cards for the LHeC and FCC-he.

On the other hand, in the LFV H channel, the dominant background arises from $pe^- \to Z(\to \tau_{e,\mu}\tau) + j_\mathrm{f}\nu$ processes. Unlike the LFV Z channel, this background does not overwhelm the signal. Consequently, choosing a small τ_h-tagging efficiency would not be advantageous since it would decrease both the signal and background event yields. To maximize the signal significance in the presence of a manageable background, we opt for a larger τ_h-tagging efficiency. This choice allows us to retain more τ-related signal events while still keeping the background under control. For the LFV H analysis, we have adopted $P_{\tau_\mathrm{h}\to\tau_\mathrm{h}} = 0.85$ for the τ_h-tagging efficiency and $P_{j\to\tau_\mathrm{h}} = 0.05$ [75].

We compute the signal significance $\mathcal{S}$ taking into account the uncertainty in the background, defined by [76]

$$\mathcal{S} = \left[2(N_\mathrm{s} + N_\mathrm{b})\log\left(\frac{(N_\mathrm{s}+N_\mathrm{b})(N_\mathrm{b}+\delta^2_\mathrm{bg})}{N_\mathrm{b}^2 + (N_\mathrm{s}+N_\mathrm{b})\delta^2_\mathrm{bg}}\right)\right. \\ \left. - \frac{2N_\mathrm{b}^2}{\delta_b^2}\log\left(1 + \frac{\delta^2_\mathrm{bg}N_\mathrm{s}}{N_\mathrm{b}(N_\mathrm{b}+\delta^2_\mathrm{bg})}\right)\right]^{1/2}, \tag{13}$$

where N_s is the number of signal events, N_b is the number of background events, and $\delta_\mathrm{bg} = \Delta_\mathrm{bg}N_\mathrm{b}$ is the uncertainty in the background yields.

A. Results of the LFV Z

For a benchmark point, we consider the following values:

$$C^L_{\tau e} = C^R_{\tau e} = 10^{-3}, \qquad P_e = 0. \tag{14}$$

Focusing on the LHeC first, we generated 5×10^5 events for the signal, 3.25×10^7 for $jj\nu$, 1.25×10^7 for $W^- + j_\mathrm{f}\nu$, and 1.25×10^7 for $Z + j_\mathrm{f}\nu$ at the MadGraph level. To account for the detector effects, we simulated the events using PYTHIA and DELPHES. Afterward, we applied the basic selection criteria, which require at least one τ_h jet and one QCD jet

---

[3] The DELPHES cards specialized for the LHeC and FCC-he can be found in the GitHub repository https://github.com/delphes/delphes/tree/master/cards.

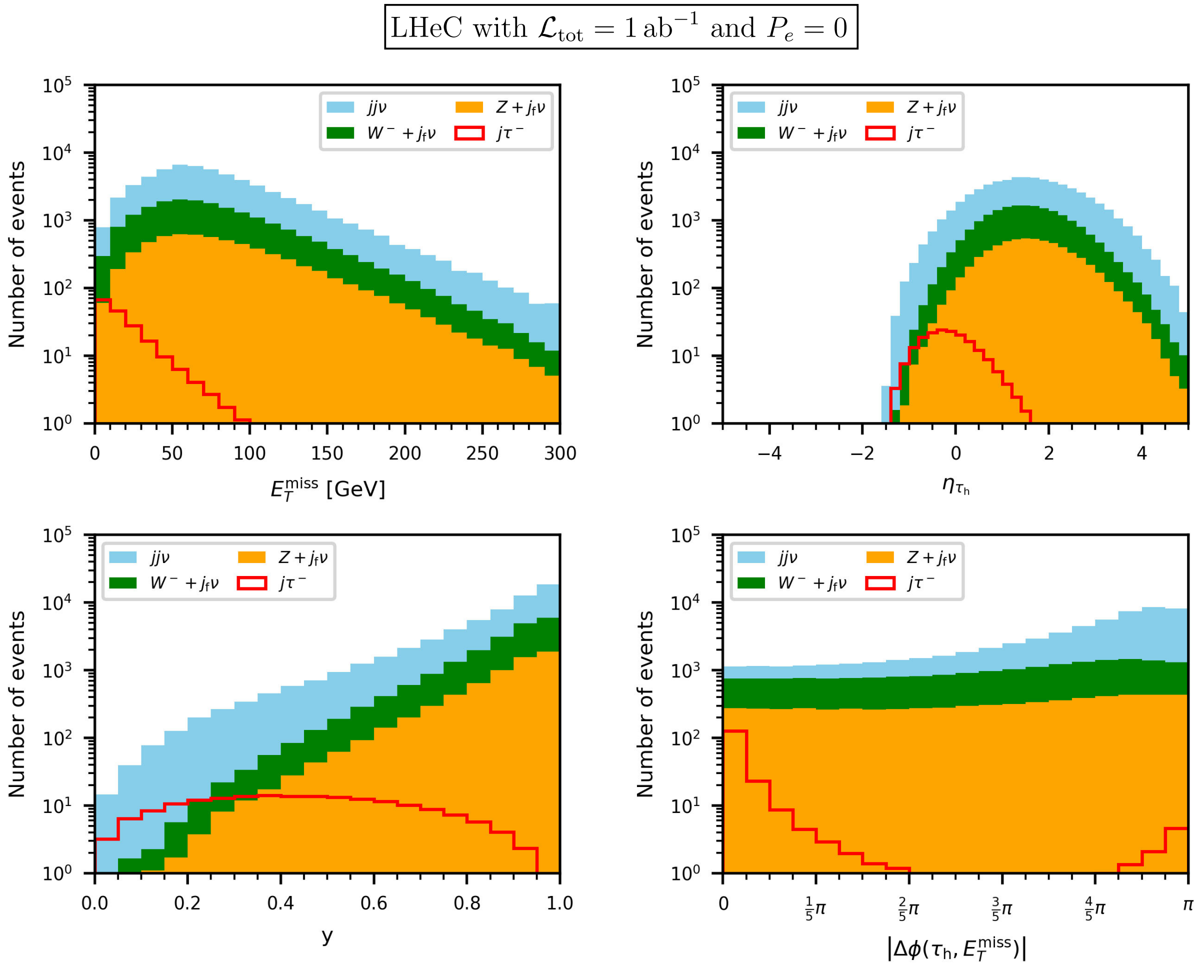

FIG. 2. Kinematic distributions for the signal of $pe^- \to j_f\tau^-$ and the corresponding backgrounds about missing transverse energy E_T^{miss} (top-left), η_{τ_h} (top-right), y (bottom-left), $|\Delta\phi(\tau_h, E_T^{\text{miss}})|$ (bottom-right) at the LHeC with the total integrated luminosity of $\mathcal{L}_{\text{tot}} = 1$ ab^{-1} and $P_e = 0$. The signal is for $C_{\tau e}^L = C_{\tau e}^R = 10^{-3}$. The results are based on the dataset after the basic selection described in the text. The various background contributions are overlaid, creating a stacked representation, while the anticipated signal is depicted by the red solid line.

(i.e., non-τ_h jet) with transverse momentum $p_T^{\tau_h,j} > 20$ GeV and pseudorapidity $|\eta_{\tau_h,j}| < 5$. We repeated the same procedure for the FCC-he.

In order to devise an optimal strategy for the cut-based analysis, it is crucial to examine various kinematic distributions. In Fig. 2, we present selected distributions after applying the basic selection criteria at the LHeC[4] with $\mathcal{L}_{\text{tot}} = 1$ ab^{-1} and $P_e = 0$. The contributions from different backgrounds are stacked on top of each other, while the expected signal for $C_{\tau e}^{L/R} = 10^{-3}$ is depicted by the red solid line. The kinematic variables for the distributions include E_T^{miss} (top-left), η_{τ_h} (top-right), y (bottom-left), and $|\Delta\phi(\tau_h, E_T^{\text{miss}})|$ (bottom-right). Here y is one of the variables used in deep inelastic scattering, defined as

$$y = \frac{p_p \cdot (p_e - p_{\tau_h})}{p_p \cdot p_e}, \tag{15}$$

where p_p represents the four-momentum of the proton beam. For the azimuthal angle difference, $|\Delta\phi(\tau_h, E_T^{\text{miss}})|$, we take the absolute value to cover the physical range $[0, \pi]$ from collinear to back-to-back configurations.

The distribution of E_T^{miss} exhibits a distinct difference between the signal and backgrounds. In the signal, it shows a monotonic decrease since E_T^{miss} is solely attributed to the neutrino from $\tau \to \tau_h\nu_\tau$ decays. In contrast, the CC backgrounds, which involve the production of a prompt neutrino, display a bump structure in the E_T^{miss} distribution, peaked around $E_T^{\text{miss}} \sim 65$ GeV. Therefore, applying an appropriate upper cut on E_T^{miss} would be an effective strategy. Furthermore, the distribution of η_{τ_h} reveals a noticeable discrepancy between the signal and backgrounds. In the

---

[4] The kinematic distributions observed at the FCC-he closely resemble those obtained at the LHeC.

TABLE IV. Cut-flow chart of the cross sections of the signal with $C^L_{\tau e} = C^R_{\tau e} = 10^{-3}$ and the corresponding backgrounds at the LHeC and the FCC-he with the unpolarized electron beam. For the significance $\mathcal{S}$, two cases of the total luminosity are considered, 1 ab^{-1} and 3 ab^{-1} for the LHeC while 1 ab^{-1} and 10 ab^{-1} for the FCC-he. We include a 10% background uncertainty.

Cross sections in units of fb at the LHeC with $P_e = 0$

Cut	Signal	$jj\nu$	$W^- + j_f\nu$	$Z + j_f\nu$	$\mathcal{S}^{10\%}_{1\ \mathrm{ab}^{-1}}$	$\mathcal{S}^{10\%}_{3\ \mathrm{ab}^{-1}}$
Basic	0.1854	40.3044	13.5870	6.4368	0.03	0.03
$Q(\tau_h) < 0$	0.1852	20.7435	12.9228	3.2324	0.05	0.05
$E_T^{\mathrm{miss}} < 10$ GeV	0.0668	0.2654	0.2207	0.0295	1.14	1.21
$\eta_{\tau_h} < 0$	0.0512	0.1293	0.0164	0.0031	2.45	2.84
$y < 0.5$	0.0465	0.0761	0.0048	0.0012	3.39	4.18
$\lvert\Delta\phi(\tau_h, E_T^{\mathrm{miss}})\rvert < \pi/10$	0.0261	0.0051	0.0007	0.0001	7.08	11.17

Cross sections in units of fb at the FCC-he with $P_e = 0$

Cut	Signal	$jj\nu$	$W^- + j_f\nu$	$Z + j_f\nu$	$\mathcal{S}^{10\%}_{1\ \mathrm{ab}^{-1}}$	$\mathcal{S}^{10\%}_{10\ \mathrm{ab}^{-1}}$
Basic	0.4904	165.6040	75.1131	37.0154	0.02	0.02
$Q(\tau_h) < 0$	0.4895	86.8901	71.2757	18.4660	0.03	0.03
$E_T^{\mathrm{miss}} < 10$ GeV	0.1454	0.8508	0.7763	0.1089	0.79	0.81
$\eta_{\tau_h} < 0$	0.1165	0.4066	0.0770	0.0127	2.00	2.17
$y < 0.3$	0.0856	0.1606	0.0068	0.0024	3.56	4.27
$\lvert\Delta\phi(\tau_h, E_T^{\mathrm{miss}})\rvert < \pi/10$	0.0470	0.0137	0.0010	0.0004	8.04	15.32

signal, the τ_h-jet originating directly from the electron beam is predominantly observed in the backward region. On the other hand, the backgrounds tend to produce more forward τ_h due to the higher energy of the proton beam compared to the electron beam.

The distributions of y also yield a distinct pattern between the signal and backgrounds. The signal distribution shows a relatively uniform spread across the range $y \in [0.05, 0.9]$, while the background distributions exhibit a peak around $y \simeq 1$. This difference can be understood by considering the definition of y in the proton rest frame, $y = (E_e^{\mathrm{rest}} - E_{\tau_h}^{\mathrm{rest}})/E_e^{\mathrm{rest}}$. In the signal events, which predominantly produce backward τ_h in the laboratory frame, the Lorentz boost into the proton rest system can result in various values of $E_{\tau_h}^{\mathrm{rest}}$ and thus the flat distribution in y. On the other hand, the backgrounds mostly feature forward τ_h in the lab frame. In the proton rest frame, the τ_h almost comes to a stop, resulting in $E_{\tau_h}^{\mathrm{rest}} \simeq 0$ and consequently $y \simeq 1$.

Let us delve into the distribution of the azimuthal angle difference between τ_h and the missing transverse momentum E_T^{miss}. In the signal, $\lvert\Delta\phi(\tau_h, E_T^{\mathrm{miss}})\rvert$ is peaked around zero.[5] This behavior arises because E_T^{miss} solely originates from $\tau \to \tau_h \nu_\tau$, which naturally leads to the collinear motion of τ_h and E_T^{miss}. For the backgrounds, on the contrary, E_T^{miss} primarily originates from prompt neutrinos. As a result, the backgrounds exhibit a larger angular separation between τ_h and $\vec{E}_T^{\mathrm{miss}}$ compared to the signal events.

Table IV illustrates the cut-flow chart, presenting the cross sections of the signal and backgrounds in units of fb at the LHeC and FCC-he, assuming an unpolarized electron beam. The signal significances are provided, taking into account a 10% background uncertainty ($\Delta_{\mathrm{bg}} = 10\%$), for two reference values of the total integrated luminosity: 1 ab^{-1} and 3 ab^{-1} at the LHeC,[6] and 1 ab^{-1} and 10 ab^{-1} at the FCC-he.

Each kinematic cut plays a crucial role in distinguishing the signal from the backgrounds. The most influential discriminator is $E_T^{\mathrm{miss}} < 10$ GeV, which increases the significance by approximately a factor of 20. By applying a series of kinematic cuts on η_{τ_h}, y, and $\lvert\Delta\phi(\tau_h, E_T^{\mathrm{miss}})\rvert$, the signal significance is further enhanced. Even with a total luminosity of $\mathcal{L}_{\mathrm{tot}} = 1\ \mathrm{ab}^{-1}$, the LFV Z couplings of $C^L_{\tau e} = C^R_{\tau e} = 10^{-3}$ can be measured with a signal significance of about 7.08 (8.04) at the LHeC (FCC-he). Increasing the LHeC (FCC-he) luminosity into 3 ab^{-1} (10 ab^{-1}) will improve the significance into $\mathcal{S}^{10\%} \simeq 11.2(15.3)$.

To explore the maximum sensitivity of the LHeC and FCC-he in probing the LFV Z, we extend our analysis by

---

[5] We also observe a smaller peak around $\lvert\Delta\phi(\tau_h, E_T^{\mathrm{miss}})\rvert \simeq \pi$ in the signal. This feature emerges due to the adoption of a relatively lower tagging efficiency $P_{\tau_h \to \tau_h} = 0.4$ and the requirement of having one τ_h and one QCD jet in the basic selection. In the signal events with $\lvert\Delta\phi(\tau_h, E_T^{\mathrm{miss}})\rvert \simeq \pi$, the object initially tagged as τ_h is a QCD jet, and the object initially tagged as j is τ_h in fact, as confirmed by $\lvert\Delta\phi(j, E_T^{\mathrm{miss}})\rvert \simeq 0$.

[6] While the CDR of the LHeC specifies a total luminosity of 1 ab^{-1}, we additionally calculated the significance for $\mathcal{L}_{\mathrm{tot}} = 3\ \mathrm{ab}^{-1}$ to demonstrate the potential gains achievable by tripling the luminosity.

employing a multivariate analysis approach. We utilized the boosted decision tree (BDT) algorithm [63], harnessed through the highly effective extreme gradient boosting (XGBOOST) package [77]. XGBOOST is one of the most powerful machine learning algorithms, showing its superiority over other methods, such as deep neural networks and support vector machines. Its exceptional performance can be primarily attributed to its unique ensemble learning techniques, most notably gradient boosting. The remarkable success of XGBOOST is exemplified by its triumphs in esteemed Kaggle competitions [78,79]. Within the particle physics community, XGBOOST has recently gained popularity and is actively being applied in various contexts, including the analysis of the SM Higgs boson [80–84], dark matter [85], vector quarks [86], a composite pseudoscalar [87], and the new strategies for faster event generation [88]. In our study, we utilized XGBOOST as a binary classifier.

For training the model, we generated 5×10^5 signal events, 3.25×10^7 for $jj\nu$, 1.25×10^7 for $W^- + j_f\nu$, and 1.25×10^7 for $Z + j_f\nu$ at the MadGraph level. The dataset was then processed through PYTHIA and DELPHES. After applying the basic selection, we divided the dataset into three parts, 52.5% for training, 30% for testing, and 17.5% for validating the algorithm. We use the following 11 observables as inputs for the BDT analysis:

$$\begin{gathered} E_T^{\text{miss}}, \quad \sqrt{-q^2}, \quad \eta_{\tau_h}, \quad \eta_j, \quad p_T^{\tau_h}, \quad p_T^j, \\ |\Delta\phi(\tau_h, j)|, \quad |\Delta\phi(\tau_h, j)|, \quad \Delta R(\tau_h, j), \quad x, \quad y, \end{gathered} \tag{16}$$

where q^2 and x are defined by

$$q^2 = (p_e - p_{\tau_h})^2, \qquad x = -\frac{q^2}{2p_p\cdot(p_e - p_{\tau_h})}. \tag{17}$$

We implemented several strategies to enhance the performance of the BDT. First, we used the area under the receiver operating characteristic curve to measure the BDT performance because there exists a significant imbalance between the signal and background samples. Second, we addressed the issue of determining the optimal stopping point for the boosting rounds to prevent overfitting and ensure the generalization of the model to unseen test samples. To accomplish this, we incorporated a validation set and continuously monitored its performance during the training process. If a noticeable decline in the validation performance was observed, it served as an indicator to stop the training. In our implementation, we set `early_stopping_rounds=3`. For the BDT output, we used the default settings in XGBOOST for binary classification tasks, employing the `binary:logistic` objective function, which represents the predicted probabilities of the positive class.

In Fig. 3, we present the normalized distributions of the signal and backgrounds against the BDT score (left panel) and the *raw* untransformed `logit` values in XGBOOST for the signal process of $pe^- \to j_f\tau^-$ at the LHeC with $P_e = 0$. We show the results exclusively from the testing dataset, which remains unseen by the model during the training and validation stages. The distribution against the BDT scores clearly shows a distinct separation between the signal and

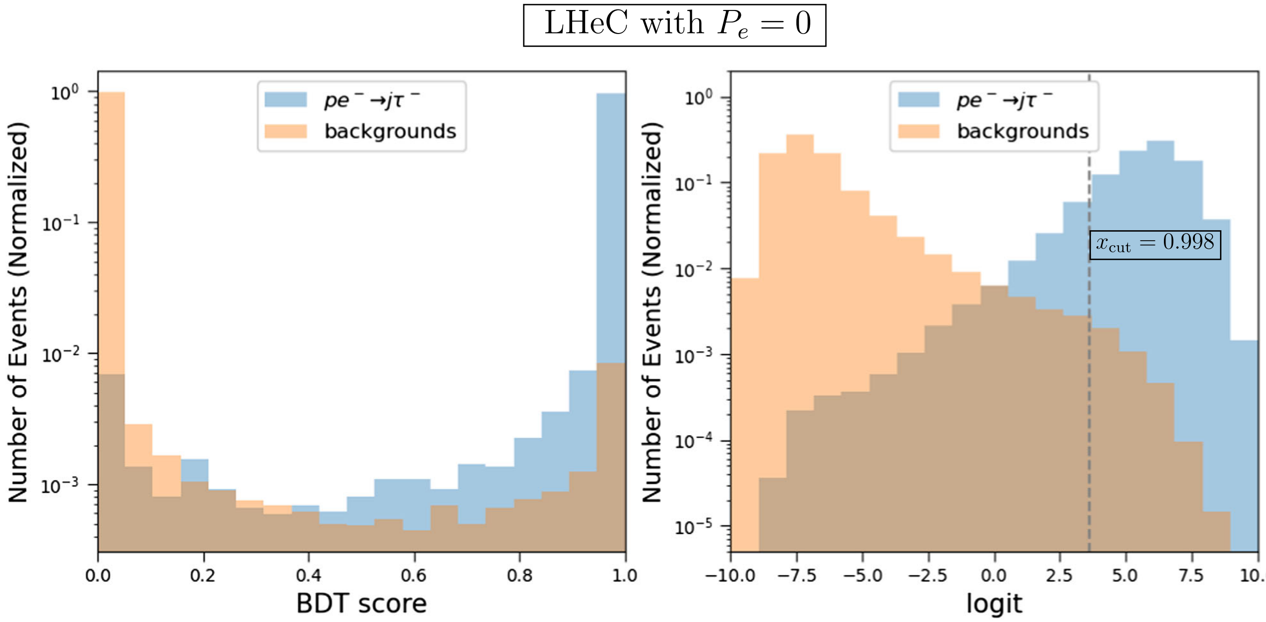

FIG. 3. Normalized signal and background distributions against the BDT score (left panel) and the raw untransformed `logit` values in XGBOOST for the signal process of $pe^- \to j_f\tau^-$. We consider the LHeC with $P_e = 0$. The results are based solely on the testing dataset after the basic selection described in the text.

TABLE V. The results of the BDT analysis for the signals of $pe^- \to \tau^- j_\mathrm{f}$ via the LFV Z with $C^L_{\tau e} = C^R_{\tau e} = 10^{-3}$ at the LHeC and FCC-he with $P_e = 0$, including 10% background uncertainty. Here N_s (N_b) is the number of signal (background) events and x_cut is the cut on the BDT output of the testing dataset.

$pe^- \to \tau^- j_\mathrm{f}$ via the LFV Z with $C^L_{\tau e} = C^R_{\tau e} = 10^{-3}$									
LHeC with $P_e = 0$					FCC-he with $P_e = 0$				
$\mathcal{L}_\mathrm{tot}$	x_cut	N_s	N_b	$\mathcal{S}^{10\%}$	$\mathcal{L}_\mathrm{tot}$	x_cut	N_s	N_b	$\mathcal{S}^{10\%}$
1 ab^{-1}	0.997	104.4	24.3	12.3	1 ab^{-1}	0.998	202.5	71.0	12.4
	0.900	192.2	405.0	3.76		0.900	494.8	1822.5	2.44
3 ab^{-1}	0.997	313.2	73.0	16.8	10 ab^{-1}	0.999	1001.8	194.8	22.4
	0.900	576.5	1214.9	4.01		0.900	4948.5	18224.6	2.50

backgrounds. Furthermore, we found that the results at the FCC-he are similar to those at the LHeC.

In Table V, we present the results of the BDT analysis for the signals of the LFV Z at the LHeC and FCC-he with $P_e = 0$ and a 10% background uncertainty. Two cases of the total integrated luminosity are considered, 1 ab^{-1} and 3 ab^{-1} for the LHeC while 1 ab^{-1} and 10 ab^{-1} for the FCC-he. The table includes the BDT score cut x_cut, the number of the signal events N_s, and the number of the total backgrounds N_b. The BDT score cut x_cut is selected to maximize the signal significance [66,89–91] while ensuring that at least 10 background events survive. The results clearly demonstrate the improvement achieved through the multivariate approach. The significance increases by about 74% (54%) at the LHeC (FCC-he) with $\mathcal{L}_\mathrm{tot} = 1\ \mathrm{ab}^{-1}$. To showcase the performance of our chosen x_cut, we also provide the results for a reference value of $x_\mathrm{cut} = 0.9$ in the table. This additional information allows readers to better understand the effect of different BDT score cuts and provides a basis for comparison to assess the robustness of our analysis.

Before proceeding to the next topic, it is essential to address potential concerns about extreme values of x_cut. The BDT scores are obtained by applying the Softmax function to the raw `logit` scores. Consequently, judging the validity based solely on the face-value of the BDT score might not be reasonable. Moreover, it is important to note that the sharp distribution of the BDT output is a characteristic feature of the Softmax function. For example, setting a BDT cut value of $x_\mathrm{cut} = 0.999$ corresponds to a signal efficiency of approximately 20%.

To better understand the underlying distributions, we have also included the distributions of the raw untransformed `logit` values in the right panel of Fig. 3. These values can be obtained by setting the objective to `binary:logitraw`. By doing so, we can assess the true characteristics of the `logit` scores and draw more meaningful conclusions. In the plot, the vertical dashed line corresponds to the BDT score cut $x_\mathrm{cut} = 0.998$, which not only demonstrates a satisfactory signal efficiency but also exhibits a moderate `logit` value.

Let us derive upper bounds on $\mathrm{Br}(Z \to e^\pm \tau^\mp)$ based on our results. Although $pe^- \to j_\mathrm{f}\tau^-$ is sensitive only to $C^L_{\tau e}$ and $C^R_{\tau e}$, we can convert the results of $C^{L,R}_{\tau e}$ into the limits on $\mathrm{Br}(Z \to e^\pm \tau^\mp)$ under the assumption that $|C^{L/R}_{\tau e}| = |C^{L/R}_{e\tau}|$. The results with the optimized x_cut in Table V yield the 2σ upper bounds on $\mathrm{Br}(Z \to e^\pm \tau^\mp)$ as

$$\mathrm{Br}(Z \to e^\pm \tau^\mp)|_\mathrm{LHeC} < \begin{cases} 2.22 \times 10^{-7} & \text{for } \mathcal{L}_\mathrm{tot} = 1\ \mathrm{ab}^{-1}; \\ 1.49 \times 10^{-7} & \text{for } \mathcal{L}_\mathrm{tot} = 3\ \mathrm{ab}^{-1}; \end{cases}$$
$$\mathrm{Br}(Z \to e^\pm \tau^\mp)|_\text{FCC-he} < \begin{cases} 2.27 \times 10^{-7} & \text{for } \mathcal{L}_\mathrm{tot} = 1\ \mathrm{ab}^{-1}; \\ 9.91 \times 10^{-8} & \text{for } \mathcal{L}_\mathrm{tot} = 10\ \mathrm{ab}^{-1}. \end{cases} \tag{18}$$

If we use the reference value $x_\mathrm{cut} = 0.9$, the upper bounds on the branching ratios change into $\mathrm{Br}(Z \to e^\pm \tau^\mp)|_\mathrm{LHeC} < 9.75 \times 10^{-7}$ and $\mathrm{Br}(Z \to e^\pm \tau^\mp)|_\text{FCC-he} < 1.57 \times 10^{-6}$ with $\mathcal{L}_\mathrm{tot} = 1\ \mathrm{ab}^{-1}$.

The results at the LHeC are indeed impressive, especially when compared to the prospects at the HL-LHC. The recent bound set by the ATLAS Collaboration [55] with a total luminosity of 139 fb^{-1} is $\mathrm{Br}(Z \to e\tau) < 5.0 \times 10^{-6}$. If we extrapolate this bound to the HL-LHC with $\mathcal{L}_\mathrm{tot} = 3\ \mathrm{ab}^{-1}$ but no background uncertainty, the expected limit becomes $\mathrm{Br}(Z \to e\tau)|_\text{HL−LHC} \lesssim 1.08 \times 10^{-6}$. Notably, the LHeC exhibits an improvement by a factor of about five with respect to the HL-LHC. Considering that both the HL-LHC and LHeC are expected to complete their programs around the same timescale, it is crucial not to overlook the potential of the LHeC in probing LFV in Z boson decays.

In contrast, the bounds obtained at the FCC-he do not experience significant improvement, despite the substantial increase in proton beam energy. This suggests that alternative strategies should be explored to effectively probe LFV in Z boson decays at the FCC-he. One promising approach is to raise the electron beam energy into 120 GeV [92]. Therefore, serious consideration should be given to the option of a higher electron beam energy, especially if our primary goal at the FCC-he is to achieve a more comprehensive exploration of BSM signals.

Finally, we discuss the limitations and potential of the *indirect* probe of the LFV Z decays. Although we may observe the BSM signal of $pe^- \to j_f\tau^-$ in the future, it does not provide conclusive evidence for LFV Z decays. The observed signal could be explained by the presence of other new particles decaying into $e\tau$ such as Z' [93], scalar neutrinos in the R-parity-violating supersymmetry models [94,95], and quantum black holes in low scale gravity [96]. While disentangling the indirect signals of the LFV Z from those of other BSM effects is beyond the scope of this paper, we provide a qualitative discussion focusing on the discrimination between LFV Z and Z' bosons.

The recent heavy resonance search for a LFV Z' boson by the CMS Collaboration [97] excluded $M_{Z'} \lesssim 4$ TeV in a benchmark scenario where the Z' boson has identical couplings to SM particles as the SM Z boson but it can decay into $e\tau$ with an assumed branching ratio of $\mathrm{Br}(Z' \to e\tau) = 0.1$ [98,99]. This exclusion bound is in line with the constraints obtained from resonant Z' searches in flavor-conserving dilepton final states, which also imply $M_{Z'} \gtrsim 4$ TeV [100]. Therefore, let us consider the specific case of $M_{Z'} = 4$ TeV in our discussion. If we assume a branching ratio of $\mathrm{Br}(Z' \to e\tau) = 2 \times 10^{-4}$, the parton-level cross section of $pe^- \to j_f\tau^-$ mediated by the t-channel Z' is almost the same as that mediated by the LFV Z boson with $C^{L/R}_{\tau e} = 10^{-3}$. Consequently, the signal rate alone cannot differentiate the indirect LFV signal of the SM Z boson from that of Z'.

However, the significant mass difference between m_Z and $M_{Z'}$ leads to distinct kinematic distributions. In Fig. 4, we highlight two distributions that exhibit pronounced differences, about η_{τ_h} (left panel) and $\sqrt{-q^2}$ (right panel) for the process of $pe^- \to j_f\tau^-$ at the LHeC with $P_e = 0$. The distributions mediated by the LFV Z and Z' are depicted by the blue and orange solid lines, respectively. Examining the η_{τ_h} distribution, we observe that the outgoing τ from the LFV Z' does not exhibit a preference for the backward direction. This is attributed to the heavy mass of Z', which results in an effective four-point interaction involving $e - \tau - q - \bar{q}$. As a result, the kinematic characteristics of the t-channel diagram are lost. In addition, significant discrepancies between the LFV Z and Z' processes are observed in the distributions of the momentum transfer, $\sqrt{-q^2}$. In the case of the LFV Z, we observe a sharper peak at a lower $\sqrt{-q^2}$ position compared with the LFV Z'. In summary, the distinctive kinematic features between the LFV Z and Z' provide optimism that it may be possible to disentangle these indirect signals when analyzing real datasets.

B. Results of the LFV Higgs boson

Exploring the LFV of the Higgs boson at electron-proton colliders poses challenges primarily due to the inherently low cross section of the Higgs production. As summarized in Table II, even at the parton level, the highest possible cross section via the CC production with $P_e = -80\%$ is merely about 145 fb (604 fb) at the LHeC (FCC-he). Considering the current bounds of $\mathrm{Br}(H \to e\tau/\mu\tau) \lesssim 10^{-3}$, the initial dataset with $\mathcal{L}_{\mathrm{tot}} = 1\ \mathrm{ab}^{-1}$ consists of only a few hundred events, leading to a limited statistical sample. Furthermore, the primary background arising from the CC production of the Z boson, followed by $Z \to \tau_e\tau_h$, shares the same Feynman diagram topology as the LFV Higgs signal. This similarity further aggravates the situation in background reduction. Despite our concerted efforts in a cut-based analysis to enhance the signal significance, we were only able to achieve a modest significance of $\mathcal{S} \simeq 1$.

To address these limitations, we turned to a multivariate analysis approach, utilizing the BDT algorithm [63] implemented through the XGBOOST package [77]. This technique

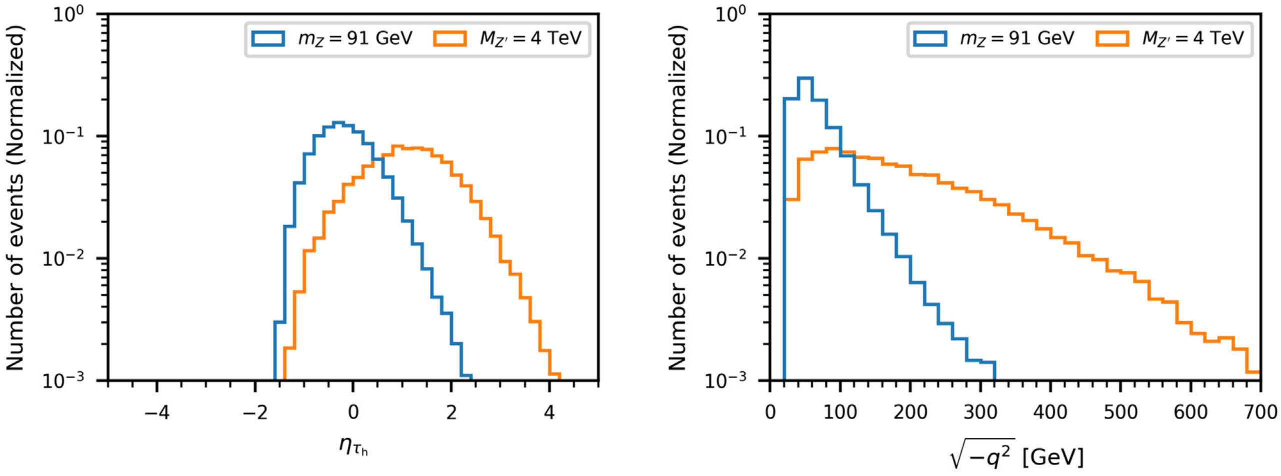

FIG. 4. Normalized distributions against η_{τ_h} (left panel) and Q (right panel) for the process of $pe^- \to j_f\tau^-$ at the LHeC with $P_e = 0$ mediated by Z (blue line) and Z' with $M_{Z'} = 4$ TeV (orange line). The results are based on the dataset after the basic selection described in the text.

allows us to exploit the correlations among multiple observables and to maximize the discrimination power between signal and background events. The reference signal points are defined by

$$\mathrm{Br}(H \to \ell^\pm \tau^\mp) = 10^{-3}, \tag{19}$$

where $\ell^\pm = e^\pm, \mu^\pm$.

Let us first discuss the LFV decay of the Higgs boson in the $e\tau$ mode. As discussed in the previous section, we concentrate on the process

$$pe^- \to H + j_\mathrm{f}\nu \to e^+\tau^- + j_\mathrm{f}\nu. \tag{20}$$

For the basic selection, we apply the following minimal conditions to avoid excessively suppressing the signal events:

(i) We require $N_{\tau_\mathrm{h}} \geq 1$, $N_e \geq 1$, and $N_j \geq 1$, where N_X is the number of the X object with $p_T > 20$ GeV, $|\eta_{j,\tau_\mathrm{h}}| < 4.5$, and $|\eta_e| < 3.5$.

(ii) We demand that the charge of the leading electron object be positive.

After the basic selection, the background from $j_e j_{\tau_\mathrm{h}} + j_\mathrm{f}\nu$ can be neglected due to the tiny mistagging probabilities of $P_{j\to e}$ and $P_{j\to\tau_\mathrm{h}}$.

To discriminate the signal from the backgrounds, we use the following 19 observables as the BDT inputs[7]:

$$\begin{aligned} &N_j, \quad N_{\tau_\mathrm{h}}, \quad N_e, \quad p_T^j, \quad p_T^{\tau_\mathrm{h}}, \quad p_T^e, \quad \eta_j, \quad \eta_{\tau_\mathrm{h}}, \quad \eta_e, \\ &\Delta R(\tau_\mathrm{h}, e), \quad \Delta R(j, \langle\tau_\mathrm{h} e\rangle), \quad \Delta\phi(\tau_\mathrm{h}, e), \quad M_{\tau_\mathrm{h} e}, \quad p_T^{\langle\tau_\mathrm{h} e\rangle}, \quad E_T^\mathrm{miss}, \\ &\Delta\phi(\vec{p}_\mathrm{miss}, \tau_\mathrm{h}), \quad \Delta\phi(\vec{p}_\mathrm{miss}, e), \quad \Delta\phi(\vec{p}_\mathrm{miss}, \langle\tau_\mathrm{h} e\rangle), \quad m_\mathrm{col}. \end{aligned} \tag{21}$$

Here $\langle\tau_\mathrm{h} e\rangle$ denotes the system consisting of $\tau_\mathrm{h}{}^-$ and e^+, of which the momentum is the vector sum of $\vec{p}_{\tau_\mathrm{h}}$ and $\vec{p}_e$. $M_{\tau_\mathrm{h} e}$ is the invariant mass of the $\langle\tau_\mathrm{h} e\rangle$ system, and $\vec{p}_\mathrm{miss}$ is the negative vector sum of the momenta of all the observed particles. m_col is the collinear mass of the $\langle\tau_\mathrm{h} e\rangle$ system, given by

$$m_\mathrm{col} = \frac{M_{\tau_\mathrm{h} e}}{\sqrt{x_{\tau_\mathrm{h}}^\mathrm{vis}}}, \tag{22}$$

where $x_{\tau_\mathrm{h}}^\mathrm{vis}$ is defined by

$$\frac{1}{x_{\tau_\mathrm{h}}^\mathrm{vis}} = 1 + \frac{\vec{p}_\mathrm{miss} \cdot \vec{p}_{\tau_\mathrm{h}}}{(p_T^{\tau_\mathrm{h}})^2}. \tag{23}$$

The area under the receiver operating characteristic curve is used as the metric to evaluate the BDT performance. The end of the training is set by `early_stopping_rounds=5` in the XGBOOST.

For $H \to \mu\tau$ mode, we consider the CC process of $H \to \mu^\pm\tau^\mp$. The final state consists of one muon, one tau lepton, one forward jet, and missing transverse energy. We do not impose any condition on the electric charge of the muon. The basic selections require $N_{\tau_\mathrm{h}} \geq 1$, $N_\mu \geq 1$, and $N_j \geq 1$ where the object satisfies $p_T > 20$ GeV, $|\eta_{j,\tau_\mathrm{h}}| < 4.5$, and $|\eta_\mu| < 3.5$. As BDT inputs, we used the same kinematic observables in Eq. (21) with the positron replaced by the muon.

Let us outline our simulation procedures for the LHeC first. For $H \to e^+\tau^-$ mode, we generated 2.0×10^6 events for the signal and 2.0×10^7 events for each background. The training dataset consisted of 3.3×10^5 events for the signal and 3.5×10^5 events for the background. Similarly, for $H \to \mu^\pm\tau^\mp$, we generated 2.0×10^6 signal events and 2.0×10^7 background events, followed by training with 6.7×10^5 signal events and 7.2×10^5 background events. The dataset was divided into 60% for training, 20% for testing, and 20% for validating the algorithm. The validation has been successfully accomplished.

To demonstrate the performance of our approach, we present in Fig. 5 the normalized distributions of the signal and backgrounds against the BDT response at the LHeC with $P_e = -80\%$. The results are based solely on the testing dataset after the basic selection. Our dataset is sufficiently large, ensuring that the distribution from test samples closely matches that from training samples. The left panel represents the results for $H \to e^+\tau^-$, while the right panel displays the results for $H \to \mu^\pm\tau^\mp$. The plot clearly shows a distinct separation between the signal and background distributions, indicating the effectiveness of our approach in discriminating LFV signals.. We followed a similar approach for the FCC-he, where the results demonstrate a comparable behavior.

Given the rarity of our signal, it is crucial to carefully select the BDT score cut x_cut. In Fig. 6, we illustrate the signal significance as a function of x_cut for the $H \to e^+\tau^-$ process at the LHeC with $\mathcal{L}_\mathrm{tot} = 1\ \mathrm{ab}^{-1}$ and $P_e = -80\%$. We observe that as x_cut increases, the significance increases, reaching a maximum before eventually decreasing.

---

[7] In the literature, it is common practice to exclude highly correlated kinematic variables in BDT analyses. Although we observed that three of the parameters in our analysis exhibit correlations higher than 80% in the signal, we decided to include all 19 variables. Surprisingly, this choice resulted in a slight improvement of about $\mathcal{O}(1)\%$ in the BDT performance.

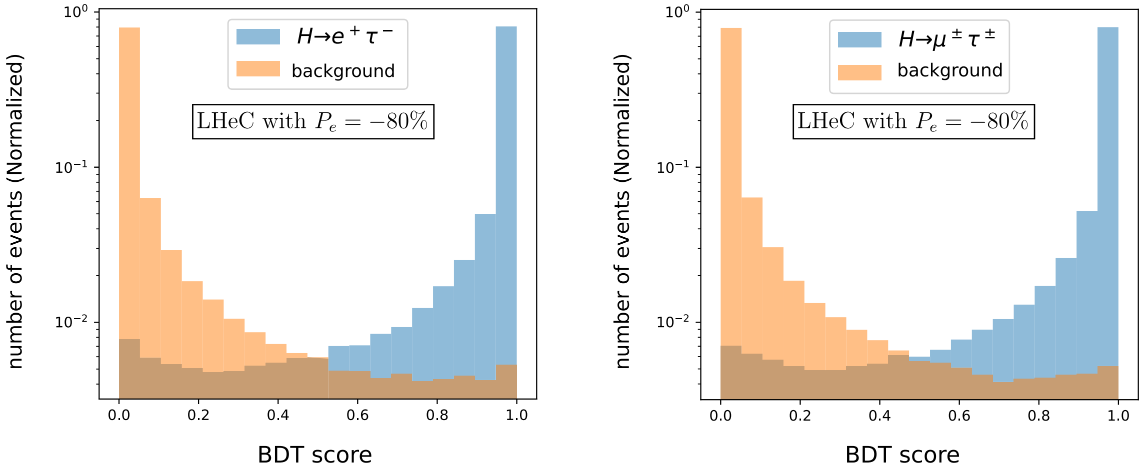

FIG. 5. Normalized signal and background distributions against BDT scores. The left panel is for $H \to e^+\tau^-$ and the right panel is for $H \to \mu^\pm\tau^\mp$ with $\mathrm{Br}(H \to e^\pm\tau^\mp/\mu^\pm\tau^\mp) = 10^{-3}$ at the LHeC with $P_e = -80\%$. The results are based solely on the testing dataset after the basic selection.

We select x_{cut} to maximize the significance while ensuring that at least one background event remains.

Brief comments are warranted on the decreasing behavior of the significance as $x_{\mathrm{cut}} \to 1$, which corresponds to the limit $N_\mathrm{b} \to 0$. In Eq. (13), the significance expression exhibits divergence as N_b approaches 0, which might seem inconsistent with the findings shown in Fig. 6. However, this divergence is a consequence of the incorrect assumption that N_s remains fixed even in the limit of $N_\mathrm{b} \to 0$, which is not reflective of real-world high-energy collider experiments. In practice, the background events can be almost entirely eliminated only when we impose very stringent cuts. However, this stringent filtering also leads to a comparable reduction in the signal events. As a result, the significance decreases rather than diverging.

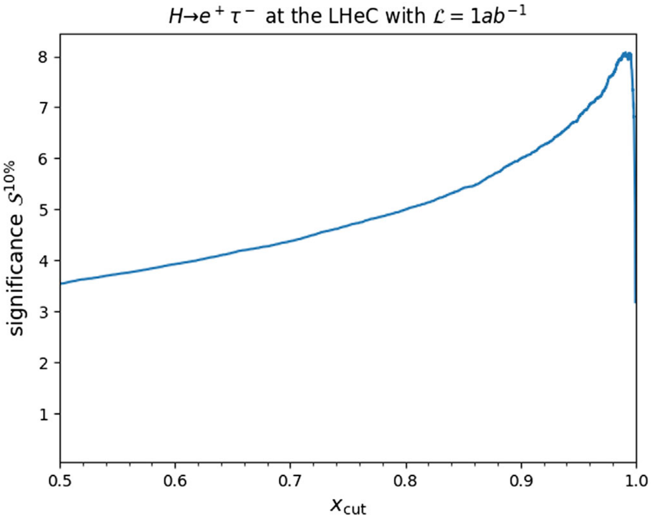

FIG. 6. Significance of the signal $H \to e^+\tau^-$ against the BDT score cut x_{cut} at the LHeC with $P_e = -80\%$ and the total luminosity of 1 ab^{-1}. We include a 10% background uncertainty.

To illustrate this point, let us consider an equivalent scenario of $N_\mathrm{b} \ll 1$ by decreasing the luminosity. Suppose we start with a given luminosity $\mathcal{L}^0_{\mathrm{tot}}$ and have $N_\mathrm{b} = 1$ and $N_\mathrm{s} = 1000$, resulting in a significance of 108. Now, if we reduce the luminosity to $0.01\mathcal{L}^0_{\mathrm{tot}}$ so that N_b takes on a very small value, both N_s and N_b decrease. As a result, the significance is reduced to 10.8, clearly illustrating a decrease rather than an increase.

In Table VI, we present the results of the BDT analysis for the LFV H decays, including the values of x_{cut}, N_s, N_b, and the significances for the signals of $H \to e^+\tau^-$ and $H \to \mu^\pm\tau^\mp$ with $\mathrm{Br}(H \to e\tau/\mu\tau) = 10^{-3}$ at the LHeC and FCC-he. We provide two sets of results: one based on the optimal x_{cut} obtained by maximizing the significance while ensuring at least one background event, and the other using a reference value of $x_{\mathrm{cut}} = 0.9$. In our analysis, we account for a 10% background uncertainty. We also consider two cases of the total integrated luminosity: 1 ab^{-1} and 3 ab^{-1} for the LHeC, and 1 ab^{-1} and 10 ab^{-1} for the FCC-he.

Our optimal choice of x_{cut} yields remarkably high signal significances for the LFV decay modes $H \to e\tau$ and $H \to \mu\tau$, making them sufficiently strong to claim a discovery if $\mathrm{Br}(H \to e\tau/\mu\tau) = 10^{-3}$. The LHeC with the proposed total luminosity of 1 ab^{-1} yields $\mathcal{S}^{10\%} \simeq 7.6$ for $H \to e^+\tau^-$ and $\mathcal{S}^{10\%} \simeq 11.0$ for $H \to \mu^\pm\tau^\mp$. Tripling the total luminosity into $\mathcal{L}_{\mathrm{tot}} = 3\ \mathrm{ab}^{-1}$ enhances the significance proportional to $\sqrt{\mathcal{L}_{\mathrm{tot}}}$ even with the 10% background uncertainty. It is attributed to the very small background events ($N_\mathrm{b} \simeq 1$). At the FCC-he with the total luminosity of 1 ab^{-1}, the significances are much higher: $\mathcal{S}^{10\%}_{1\ \mathrm{ab}^{-1}} \simeq 15$ for $H \to e^+\tau^-$ and $\mathcal{S}^{10\%}_{1\ \mathrm{ab}^{-1}} \simeq 21$ for $H \to \mu^\pm\tau^\mp$. The improvement from the high luminosity of 10 ab^{-1} is impressive. We can accommodate $\mathcal{S}^{10\%}_{1\ \mathrm{ab}^{-1}} \simeq 39$ for $H \to e^+\tau^-$ and $\mathcal{S}^{10\%}_{1\ \mathrm{ab}^{-1}} \simeq 50$ for $H \to \mu^\pm\tau^\mp$. Notably, the results for a reference value of $x_{\mathrm{cut}} = 0.9$ do not show a substantial decrease in the

TABLE VI. The BDT analysis results for the signals of $H \to e^+\tau^-$ and $H \to \mu^\pm\tau^\mp$ at the LHeC and FCC-he with $P_e = -80\%$, including 10% background uncertainty. Here N_s (N_b) is the number of signal (background) events and x_cut is the cut on the BDT output of the testing dataset.

$\mathrm{Br}(H \to e\tau/\mu\tau) = 10^{-3}$										
	LHeC with $P_e = -80\%$					FCC-he with $P_e = -80\%$				
	$\mathcal{L}_\mathrm{tot}$	x_cut	N_s	N_b	$\mathcal{S}^{10\%}$	$\mathcal{L}_\mathrm{tot}$	x_cut	N_s	N_b	$\mathcal{S}^{10\%}$
$H \to e^+\tau^-$	1 ab^{-1}	0.978	15.4	1.0	7.61	1 ab^{-1}	0.993	47.3	1.4	15.23
		0.900	18.1	4.1	5.99		0.900	77.2	22.1	10.15
	3 ab^{-1}	0.991	38.9	1.3	13.64	10 ab^{-1}	0.993	472.5	13.9	39.19
		0.900	54.3	12.3	9.68		0.900	772.1	221.2	17.47
$H \to \mu^\pm\tau^\mp$	1 ab^{-1}	0.990	26.5	1.0	11.01	1 ab^{-1}	0.992	103.2	3.9	20.62
		0.900	36.3	8.7	8.02		0.900	156.1	45.9	12.61
	3 ab^{-1}	0.994	69.3	1.9	18.43	10 ab^{-1}	0.997	713.4	13.9	49.75
		0.900	109.0	26.1	12.29		0.900	1561	459.4	18.28

signal significance, illustrating the efficiency of our analysis. This indicates that our approach remains effective even for slightly suboptimal choices of the x_cut parameter.

Based on the results with the optimal x_cut in Table VI, we calculate the 2σ upper bounds on the LFV decays of the Higgs boson as

$$\begin{aligned}
\mathrm{Br}(H \to e^\pm\tau^\mp) &< \begin{cases} 1.7(0.74) \times 10^{-4}, & \text{at the LHeC with } \mathcal{L}_\mathrm{tot} = 1(3)\ \mathrm{ab}^{-1}, \\ 6.3(1.9) \times 10^{-5}, & \text{at the FCC-he with } \mathcal{L}_\mathrm{tot} = 1(10)\ \mathrm{ab}^{-1}; \end{cases} \\
\mathrm{Br}(H \to \mu^\pm\tau^\mp) &< \begin{cases} 1.0(0.49) \times 10^{-4}, & \text{at the LHeC with } \mathcal{L}_\mathrm{tot} = 1(3)\ \mathrm{ab}^{-1}, \\ 4.5(1.2) \times 10^{-5}, & \text{at the FCC-he with } \mathcal{L}_\mathrm{tot} = 1(10)\ \mathrm{ab}^{-1}. \end{cases}
\end{aligned} \tag{24}$$

It is noteworthy that the LHeC with a total luminosity of 1 ab^{-1} can establish higher sensitivities to the LFV decay branching ratios of the Higgs boson than the HL-LHC with $\mathcal{L}_\mathrm{tot} = 3\ \mathrm{ab}^{-1}$. Furthermore, the performance of the FCC-he is particularly remarkable, as the dataset with $\mathcal{L}_\mathrm{tot} = 1\ \mathrm{ab}^{-1}$ has the capacity to probe LFV decay branching ratios of the Higgs boson as low as $\mathcal{O}(10^{-5})$. Additionally, we present the branching ratio limits for $x_\mathrm{cut} = 0.9$. The limits increase to $\mathrm{Br}(H \to e^\pm\tau^\mp)|_\mathrm{LHeC} < 2.7 \times 10^{-4}$, $\mathrm{Br}(H \to e^\pm\tau^\mp)|_\text{FCC-he} < 1.5 \times 10^{-4}$, $\mathrm{Br}(H \to \mu^\pm\tau^\mp)|_\mathrm{LHeC} < 1.9 \times 10^{-4}$, and $\mathrm{Br}(H \to \mu^\pm\tau^\mp)|_\text{FCC-he} < 1.1 \times 10^{-4}$ with $\mathcal{L}_\mathrm{tot} = 1\ \mathrm{ab}^{-1}$.

IV. CONCLUSIONS

We have conducted a comprehensive investigation into the potential of the LHeC and FCC-he for detecting lepton flavor violation (LFV) phenomena of the Z and Higgs bosons. For our analysis, we considered collision energies of $E_e = 50$ GeV and $E_p = 7$ TeV for the LHeC and $E_e = 60$ GeV and $E_p = 50$ TeV for the FCC-he. We found that electron-proton colliders are well-suited for detecting LFV phenomena thanks to negligible pileups, small QCD backgrounds, and the feasibility to distinguish the charged-current from neutral current processes.

For the Z LFV study, we focused on the indirect probe $pe^- \to j_\mathrm{f}\tau^-$ mediated by the Z boson in the t-channel. Employing a conventional cut-based analysis and considering a full detector simulation with 10% background uncertainty, we have demonstrated that the LHeC with $\mathcal{L}_\mathrm{tot} = 1\ \mathrm{ab}^{-1}$ and electron beam polarization of $P_e = 0$ can yield a significance of about 7.08 if $C^L_{\tau e} = C^R_{\tau e} = 10^{-3}$, while the FCC-he with $\mathcal{L}_\mathrm{tot} = 1\ \mathrm{ab}^{-1}$ has a significance of about 8.04. We have extended the analysis employing a dedicated multivariate analysis utilizing the BDT algorithm with the XGBOOST package, which enhances the significances by about 74% (54%) at the LHeC (FCC-he) with $\mathcal{L}_\mathrm{tot} = 1\ \mathrm{ab}^{-1}$. Applying the optimal cut on the BDT output x_cut, we obtained 2σ bounds of $\mathrm{Br}(Z \to e\tau) \le 2.22(2.27) \times 10^{-7}$ at the LHeC (FCC-he) with $\mathcal{L}_\mathrm{tot} = 1\ \mathrm{ab}^{-1}$. Remarkably, the LHeC with a luminosity of $\mathcal{L}_\mathrm{tot} = 1\ \mathrm{ab}^{-1}$ alone exhibits higher sensitivity compared to the HL-LHC with $\mathcal{L}_\mathrm{tot} = 3\ \mathrm{ab}^{-1}$.

For the LFV studies involving the Higgs boson, we have concentrated on the direct observation of on-shell decays. Specifically, we have emphasized $H \to e^+\tau^-$ to avoid the electron-related backgrounds. To address the challenges associated with the small production cross sections of the Higgs boson at the LHeC and FCC-he, we employed a multivariate analysis utilizing the BDT algorithm with the XGBOOST package. Our analysis with the optimal $x_{\rm cut}$ yielded the 2σ bounds at the LHeC (FCC-he) with $\mathcal{L}_{\rm tot} = 1\ {\rm ab}^{-1}$ and $P_e = -80\%$ such that $\mathrm{Br}(H \to e^{\pm}\tau^{\mp}) < 1.7 \times 10^{-4} (6.3 \times 10^{-5})$ and $\mathrm{Br}(H \to \mu^{\pm}\tau^{\mp}) < 1.0 \times 10^{-4} (4.5 \times 10^{-5})$. These bounds surpass the projected sensitivities of the HL-LHC with $\mathcal{L}_{\rm tot} = 3\ {\rm ab}^{-1}$.

Our investigation into the LFV signatures of the Z and Higgs bosons has unveiled the high potential of the LHeC and FCC-he in observing these rare processes. Given the impressive outcomes of our study, we strongly endorse and support the LHeC and FCC-he programs.

ACKNOWLEDGMENTS

We express our gratitude to the referee for the invaluable comments and thought-provoking questions, which significantly enhanced the quality and impact of our paper. This paper was written as part of Konkuk University's research support program for its faculty on sabbatical leave in 2023. The work of A. J. is supported by the Institute for Basic Science (IBS) under the project code, IBS-R018-D1. The work of J. K., S. L., J. S., and D. W. is supported by the National Research Foundation of Korea, Grant No. NRF-2022R1A2C1007583.

---

[1] G. Aad *et al.* (ATLAS Collaboration), Observation of a new particle in the search for the Standard Model Higgs boson with the ATLAS detector at the LHC, Phys. Lett. B **716**, 1 (2012).

[2] S. Chatrchyan *et al.* (CMS Collaboration), Combined results of searches for the standard model Higgs boson in pp collisions at $\sqrt{s} = 7$ TeV, Phys. Lett. B **710**, 26 (2012).

[3] J. F. Navarro, C. S. Frenk, and S. D. M. White, The structure of cold dark matter halos, Astrophys. J. **462**, 563 (1996).

[4] G. Bertone, D. Hooper, and J. Silk, Particle dark matter: Evidence, candidates and constraints, Phys. Rep. **405**, 279 (2005).

[5] S. Dimopoulos and G. F. Giudice, Naturalness constraints in supersymmetric theories with nonuniversal soft terms, Phys. Lett. B **357**, 573 (1995).

[6] K. L. Chan, U. Chattopadhyay, and P. Nath, Naturalness, weak scale supersymmetry and the prospect for the observation of supersymmetry at the Tevatron and at the CERN LHC, Phys. Rev. D **58**, 096004 (1998).

[7] N. Craig, A. Katz, M. Strassler, and R. Sundrum, Naturalness in the dark at the LHC, J. High Energy Phys. 07 (2015) 105.

[8] G. Degrassi, S. Di Vita, J. Elias-Miro, J. R. Espinosa, G. F. Giudice, G. Isidori, and A. Strumia, Higgs mass and vacuum stability in the standard model at NNLO, J. High Energy Phys. 08 (2012) 098.

[9] G. W. Bennett *et al.* (Muon g-2 Collaboration), Final report of the muon E821 anomalous magnetic moment measurement at BNL, Phys. Rev. D **73**, 072003 (2006).

[10] B. Abi *et al.* (Muon g-2 Collaboration), Measurement of the Positive Muon Anomalous Magnetic Moment to 0.46 ppm, Phys. Rev. Lett. **126**, 141801 (2021).

[11] T. Aoyama, T. Kinoshita, and M. Nio, Theory of the anomalous magnetic moment of the electron, Atoms **7**, 28 (2019).

[12] T. Aaltonen *et al.* (CDF Collaboration), High-precision measurement of the W boson mass with the CDF II detector, Science **376**, 170 (2022).

[13] A. M. Coutinho, A. Crivellin, and C. A. Manzari, Global Fit to Modified Neutrino Couplings and the Cabibbo-Angle Anomaly, Phys. Rev. Lett. **125**, 071802 (2020).

[14] Y. Grossman, E. Passemar, and S. Schacht, On the statistical treatment of the Cabibbo angle anomaly, J. High Energy Phys. 07 (2020) 068.

[15] B. Belfatto, R. Beradze, and Z. Berezhiani, The CKM unitarity problem: A trace of new physics at the TeV scale?, Eur. Phys. J. C **80**, 149 (2020).

[16] CMS Collaboration, Search for new resonances in the diphoton final state in the mass range between 70 and 110 GeV in pp collisions at $\sqrt{s} = 8$ and 13 TeV, [http://cds.cern.ch/record/2285326].

[17] S. von Buddenbrock, A. S. Cornell, A. Fadol, M. Kumar, B. Mellado, and X. Ruan, Multi-lepton signatures of additional scalar bosons beyond the Standard Model at the LHC, J. Phys. G **45**, 115003 (2018).

[18] A. Crivellin, Y. Fang, O. Fischer, A. Kumar, M. Kumar, E. Malwa *et al.*, Accumulating evidence for the associate production of a neutral scalar with mass around 151 GeV, arXiv:2109.02650.

[19] S. Buddenbrock, A. S. Cornell, Y. Fang, A. Fadol Mohammed, M. Kumar, B. Mellado, and K. G. Tomiwa, The emergence of multi-lepton anomalies at the LHC and their compatibility with new physics at the EW scale, J. High Energy Phys. 10 (2019) 157.

[20] S. L. Glashow, J. Iliopoulos, and L. Maiani, Weak interactions with lepton-hadron symmetry, Phys. Rev. D **2**, 1285 (1970).

[21] A. Pilaftsis, Lepton flavor nonconservation in H0 decays, Phys. Lett. B **285**, 68 (1992).

[22] J. G. Korner, A. Pilaftsis, and K. Schilcher, Leptonic flavor changing Z0 decays in $\mathrm{SU}(2) \times \mathrm{U}(1)$ theories with right-handed neutrinos, Phys. Lett. B **300**, 381 (1993).

[23] J. I. Illana and T. Riemann, Charged lepton flavor violation from massive neutrinos in Z decays, Phys. Rev. D **63**, 053004 (2001).

[24] E. Arganda, A. M. Curiel, M. J. Herrero, and D. Temes, Lepton flavor violating Higgs boson decays from massive seesaw neutrinos, Phys. Rev. D **71**, 035011 (2005).

[25] E. Arganda, M. J. Herrero, X. Marcano, and C. Weiland, Imprints of massive inverse seesaw model neutrinos in lepton flavor violating Higgs boson decays, Phys. Rev. D **91**, 015001 (2015).

[26] E. Arganda, M. J. Herrero, X. Marcano, and C. Weiland, Enhancement of the lepton flavor violating Higgs boson decay rates from SUSY loops in the inverse seesaw model, Phys. Rev. D **93**, 055010 (2016).

[27] V. De Romeri, M. J. Herrero, X. Marcano, and F. Scarcella, Lepton flavor violating Z decays: A promising window to low scale seesaw neutrinos, Phys. Rev. D **95**, 075028 (2017).

[28] E. Arganda, M. J. Herrero, X. Marcano, R. Morales, and A. Szynkman, Effective lepton flavor violating Hℓiℓj vertex from right-handed neutrinos within the mass insertion approximation, Phys. Rev. D **95**, 095029 (2017).

[29] M. J. Herrero, X. Marcano, R. Morales, and A. Szynkman, One-loop effective LFV $Zl_k l_m$ vertex from heavy neutrinos within the mass insertion approximation, Eur. Phys. J. C **78**, 815 (2018).

[30] J. D. Bjorken and S. Weinberg, A Mechanism for Nonconservation of Muon Number, Phys. Rev. Lett. **38**, 622 (1977).

[31] J. L. Diaz-Cruz and J. J. Toscano, Lepton flavor violating decays of Higgs bosons beyond the standard model, Phys. Rev. D **62**, 116005 (2000).

[32] E. O. Iltan and I. Turan, Lepton flavor violating $Z \to l_1^+ l_1^-$ decay in the general Higgs doublet model, Phys. Rev. D **65**, 013001 (2002).

[33] T. Nomura and P. Sanyal, Explaining Atomki anomaly and muon $g-2$ in $U(1)_X$ extended flavour violating two Higgs doublet model, J. High Energy Phys. 05 (2021) 232.

[34] J. I. Illana and M. Masip, Lepton flavor violation in Z and lepton decays in supersymmetric models, Phys. Rev. D **67**, 035004 (2003).

[35] M. Arana-Catania, E. Arganda, and M. J. Herrero, Non-decoupling SUSY in LFV Higgs decays: A window to new physics at the LHC, J. High Energy Phys. 09 (2013) 160.

[36] A. Arhrib, Y. Cheng, and O. C. W. Kong, Comprehensive analysis on lepton flavor violating Higgs boson to $\mu^\mp\tau^\pm$ decay in supersymmetry without R parity, Phys. Rev. D **87**, 015025 (2013).

[37] K. Agashe and R. Contino, Composite Higgs-mediated FCNC, Phys. Rev. D **80**, 075016 (2009).

[38] G. Perez and L. Randall, Natural neutrino masses and mixings from warped geometry, J. High Energy Phys. 01 (2009) 077.

[39] A. Azatov, M. Toharia, and L. Zhu, Higgs mediated FCNC's in warped extra dimensions, Phys. Rev. D **80**, 035016 (2009).

[40] M. E. Albrecht, M. Blanke, A. J. Buras, B. Duling, and K. Gemmler, Electroweak and flavour structure of a warped extra dimension with custodial protection, J. High Energy Phys. 09 (2009) 064.

[41] L. Calibbi, X. Marcano, and J. Roy, Z lepton flavour violation as a probe for new physics at future e^+e^- colliders, Eur. Phys. J. C **81**, 1054 (2021).

[42] A. Jueid, S. Nasri, and R. Soualah, Searching for GeV-scale Majorana dark matter: Inter spem et metum, J. High Energy Phys. 04 (2021) 012.

[43] A. Jueid and S. Nasri, Lepton portal dark matter at muon colliders: Total rates and generic features for phenomenologically viable scenarios, Phys. Rev. D **107**, 115027 (2023).

[44] L. Calibbi and G. Signorelli, Charged lepton flavour violation: An experimental and theoretical introduction, Riv. Nuovo Cimento **41**, 71 (2018).

[45] D. N. Dinh, A. Ibarra, E. Molinaro, and S. T. Petcov, The $\mu - e$ conversion in nuclei, $\mu \to e\gamma, \mu \to 3e$ decays and TeV scale see-saw scenarios of neutrino mass generation, J. High Energy Phys. 08 (2012) 125.

[46] R. Harnik, J. Kopp, and J. Zupan, Flavor violating Higgs decays, J. High Energy Phys. 03 (2013) 026.

[47] G. Blankenburg, J. Ellis, and G. Isidori, Flavour-changing decays of a 125 GeV Higgs-like particle, Phys. Lett. B **712**, 386 (2012).

[48] S. Davidson, S. Lacroix, and P. Verdier, LHC sensitivity to lepton flavour violating Z boson decays, J. High Energy Phys. 09 (2012) 092.

[49] J. Adam *et al.* (MEG Collaboration), New Constraint on the Existence of the $\mu^+ \to e^+\gamma$ Decay, Phys. Rev. Lett. **110**, 201801 (2013).

[50] ATLAS Collaboration, Search for the charged-lepton-flavor-violating decay $Z \to e\mu$ in pp collisions at $\sqrt{s} = 13$ TeV with the ATLAS detector, Phys. Rev. D **108**, 032015 (2023).

[51] M. Dam, Tau-lepton Physics at the FCC-ee circular e^+e^- Collider, SciPost Phys. Proc. **1**, 041 (2019).

[52] A. Hayrapetyan *et al.* (CMS Collaboration), Search for the lepton-flavor violating decay of the Higgs boson and additional Higgs bosons in the $e\mu$ final state in proton-proton collisions at $\sqrt{s} = 13$ TeV, arXiv:2305.18106.

[53] S. Banerjee, B. Bhattacherjee, M. Mitra, and M. Spannowsky, The lepton flavour violating Higgs decays at the HL-LHC and the ILC, J. High Energy Phys. 07 (2016) 059.

[54] Q. Qin, Q. Li, C.-D. Lü, F.-S. Yu, and S.-H. Zhou, Charged lepton flavor violating Higgs decays at future e^+e^- colliders, Eur. Phys. J. C **78**, 835 (2018).

[55] G. Aad *et al.* (ATLAS Collaboration), Search for Lepton-Flavor-Violation in Z-Boson Decays with τ-Leptons with the ATLAS Detector, Phys. Rev. Lett. **127**, 271801 (2022).

[56] G. Aad *et al.* (ATLAS Collaboration), Searches for lepton-flavour-violating decays of the Higgs boson into $e\tau$ and $\mu\tau$ in $\sqrt{s} = 13$ TeV pp collisions with the ATLAS detector, J. High Energy Phys. 07 (2023) 166.

[57] A. M. Sirunyan *et al.* (CMS Collaboration), Search for lepton-flavor violating decays of the Higgs boson in the $\mu\tau$ and $e\tau$ final states in proton-proton collisions at $\sqrt{s} = 13$ TeV, Phys. Rev. D **104**, 032013 (2021).

[58] R. K. Barman, P. S. B. Dev, and A. Thapa, Constraining lepton flavor violating Higgs couplings at the HL-LHC in the vector boson fusion channel, Phys. Rev. D **107**, 075018 (2023).

[59] J. L. Abelleira Fernandez *et al.* (LHeC Study Group), A large hadron electron collider at CERN: Report on the physics and design concepts for machine and detector, J. Phys. G **39**, 075001 (2012).

[60] O. Bruening and M. Klein, The large hadron electron collider, Mod. Phys. Lett. A **28**, 1330011 (2013).

[61] P. Agostini *et al.* (LHeC, FCC-he Study Group), The large hadron–electron collider at the HL-LHC, J. Phys. G **48**, 110501 (2021).

[62] A. Abada *et al.* (FCC Collaboration), FCC physics opportunities: Future circular collider conceptual design report volume 1, Eur. Phys. J. C **79**, 474 (2019).

[63] B. P. Roe, H.-J. Yang, J. Zhu, Y. Liu, I. Stancu, and G. McGregor, Boosted decision trees, an alternative to artificial neural networks, Nucl. Instrum. Methods Phys. Res., Sect. A **543**, 577 (2005).

[64] J. Alwall, M. Herquet, F. Maltoni, O. Mattelaer, and T. Stelzer, MadGraph5: Going beyond, J. High Energy Phys. 06 (2011) 128.

[65] R. D. Ball *et al.* (NNPDF Collaboration), Parton distributions from high-precision collider data, Eur. Phys. J. C **77**, 663 (2017).

[66] S. Antusch, A. Hammad, and A. Rashed, Probing Z' mediated charged lepton flavor violation with taus at the LHeC, Phys. Lett. B **810**, 135796 (2020).

[67] G. L. Bayatian *et al.* (CMS Collaboration), CMS technical design report, volume II: Physics performance, J. Phys. G **34**, 995 (2007).

[68] G. Bagliesi, Tau tagging at Atlas and CMS, in *Proceedings of the 17th Symposium on Hadron Collider Physics 2006 (HCP 2006)* (2007), arXiv:0707.0928.

[69] A. M. Sirunyan *et al.* (CMS Collaboration), Performance of reconstruction and identification of τ leptons decaying to hadrons and ν_τ in pp collisions at $\sqrt{s} = 13$ TeV, J. Instrum. **13**, P10005 (2018).

[70] C. Degrande, C. Duhr, B. Fuks, D. Grellscheid, O. Mattelaer, and T. Reiter, UFO—The universal FeynRules output, Comput. Phys. Commun. **183**, 1201 (2012).

[71] C. Bierlich *et al.*, A comprehensive guide to the physics and usage of PYTHIA 8.3, arXiv:2203.11601.

[72] J. de Favereau, C. Delaere, P. Demin, A. Giammanco, V. Lemaître, A. Mertens, and M. Selvaggi (DELPHES 3 Collaboration), DELPHES 3, A modular framework for fast simulation of a generic collider experiment, J. High Energy Phys. 02 (2014) 057.

[73] M. Cacciari, G. P. Salam, and G. Soyez, The anti-k_t jet clustering algorithm, J. High Energy Phys. 04 (2008) 063.

[74] M. Cacciari, G. P. Salam, and G. Soyez, FastJet user manual, Eur. Phys. J. C **72**, 1896 (2012).

[75] ATLAS Collaboration, Reconstruction, identification, and Calibration of hadronically decaying tau leptons with the ATLAS detector for the LHC Run 3 and reprocessed Run 2 data, [http://cds.cern.ch/record/2827111].

[76] G. Cowan, K. Cranmer, E. Gross, and O. Vitells, Asymptotic formulae for likelihood-based tests of new physics, Eur. Phys. J. C **71**, 1554 (2011).

[77] T. Chen and C. Guestrin, XGBoost: A scalable tree boosting system, arXiv:1603.02754.

[78] https://www.kaggle.com/code/sudalairajkumar/winning-solutions-of-kaggle-competitions.

[79] https://www.kaggle.com/code/rajiao/winning-solutions-of-kaggle-competitions.

[80] M. Aaboud *et al.* (ATLAS Collaboration), Evidence for the associated production of the Higgs boson and a top quark pair with the ATLAS detector, Phys. Rev. D **97**, 072003 (2018).

[81] A. M. Sirunyan *et al.* (CMS Collaboration), Search for nonresonant Higgs boson pair production in final states with two bottom quarks and two photons in proton-proton collisions at $\sqrt{s} = 13$ TeV, J. High Energy Phys. 03 (2021) 257.

[82] G. Aad *et al.* (ATLAS Collaboration), Search for Higgs boson pair production in the two bottom quarks plus two photons final state in pp collisions at $\sqrt{s} = 13$ TeV with the ATLAS detector, Phys. Rev. D **106**, 052001 (2022).

[83] A. M. Sirunyan *et al.* (CMS Collaboration), Measurements of $t\bar{t}H$ Production and the CP Structure of the Yukawa Interaction between the Higgs Boson and Top Quark in the Diphoton Decay Channel, Phys. Rev. Lett. **125**, 061801 (2020).

[84] A. Tumasyan *et al.* (CMS Collaboration), Analysis of the CP structure of the Yukawa coupling between the Higgs boson and τ leptons in proton-proton collisions at $\sqrt{s} = 13$ TeV, J. High Energy Phys. 06 (2022) 012.

[85] G. Aad *et al.* (ATLAS Collaboration), Search for dark matter in events with missing transverse momentum and a Higgs boson decaying into two photons in pp collisions at $\sqrt{s} = 13$ TeV with the ATLAS detector, J. High Energy Phys. 10 (2021) 013.

[86] S. Dasgupta, R. Pramanick, and T. S. Ray, Broad toplike vector quarks at LHC and HL-LHC, Phys. Rev. D **105**, 035032 (2022).

[87] A. S. Cornell, A. Deandrea, B. Fuks, and L. Mason, Future lepton collider prospects for a ubiquitous composite pseudoscalar, Phys. Rev. D **102**, 035030 (2020).

[88] F. Bishara and M. Montull, Machine learning amplitudes for faster event generation, Phys. Rev. D **107**, L071901 (2023).

[89] Z. Kang, J. Li, and M. Zhang, Uncover compressed supersymmetry via boosted bosons from the heavier stop/sbottom, Eur. Phys. J. C **77**, 371 (2017).

[90] D. Wang, L. Wu, and M. Zhang, Hunting for top partner with a new signature at the LHC, Phys. Rev. D **103**, 115017 (2021).

[91] A. Adhikary, N. Chakrabarty, I. Chakraborty, and J. Lahiri, Probing the $H^\pm W^\mp Z$ interaction at the high energy upgrade of the LHC, Eur. Phys. J. C **81**, 554 (2021).

[92] A. Jueid, J. Kim, S. Lee, and J. Song, Studies of nonresonant Higgs pair production at electron-proton colliders, Phys. Lett. B **819**, 136417 (2021).

[93] P. Langacker, The physics of heavy Z' gauge bosons, Rev. Mod. Phys. **81**, 1199 (2009).

[94] G. R. Farrar and P. Fayet, Phenomenology of the production, decay, and detection of new hadronic states associated with supersymmetry, Phys. Lett. **76B**, 575 (1978).

[95] R. Barbier *et al.*, R-parity violating supersymmetry, Phys. Rep. **420**, 1 (2005).

[96] D. M. Gingrich, Quantum black holes with charge, colour, and spin at the LHC, J. Phys. G **37**, 105008 (2010).

[97] A. Tumasyan *et al.* (CMS Collaboration), Search for heavy resonances and quantum black holes in $e\mu$, $e\tau$, and $\mu\tau$ final states in proton-proton collisions at $\sqrt{s} = 13$ TeV, J. High Energy Phys. 05 (2023) 227.

[98] A. M. Sirunyan *et al.* (CMS Collaboration), Search for lepton-flavor violating decays of heavy resonances and quantum black holes to $e\mu$ final states in proton-proton collisions at $\sqrt{s} = 13$ TeV, J. High Energy Phys. 04 (2018) 073.

[99] M. Aaboud *et al.* (ATLAS Collaboration), Search for lepton-flavor violation in different-flavor, high-mass final states in pp collisions at $\sqrt{s} = 13$ TeV with the ATLAS detector, Phys. Rev. D **98**, 092008 (2018).

[100] G. Aad *et al.* (ATLAS Collaboration), Search for high-mass dilepton resonances using 139 fb^{-1} of pp collision data collected at $\sqrt{s} = 13$ TeV with the ATLAS detector, Phys. Lett. B **796**, 68 (2019).